Journal of
*Marine Science
and Engineering*

MDPI

Article

Numerical Assessment on the Dynamic Behaviour of Submarine Hoses Attached to CALM Buoy Configured as Lazy-S under Water Waves

Chiemela Victor Amaechi [1,2,*], Facheng Wang [3,*] and Jianqiao Ye [1,*]

[1] Department of Engineering, Lancaster University, Lancaster LA1 4YR, UK
[2] Standards Organisation of Nigeria (SON), 52 Lome Crescent, Wuse Zone 7, Abuja 900287, Nigeria
[3] Department of Civil Engineering, Tsinghua University, Beijing 100084, China
[*] Correspondence: c.amaechi@lancaster.ac.uk or chiemelavic@gmail.com (C.V.A.); wangfacheng@tsinghua.edu.cn (F.W.); j.ye2@lancaster.ac.uk (J.Y.)

Abstract: Recent design challenges in ocean observations, energy storage, offloading/discharging, and loading operations in both the offshore-renewable industry have led to advances in the application of catenary anchor leg moorings (CALM) buoys. Due to different seabed profiles, soil stiffness and environmental conditions, there is the need for numerical assessment to investigate the behaviour of the submarine hoses, based on the structural and hydrodynamic behaviour. In this study, experimental and numerical investigations are carried out on the dynamic behaviour of the submarine hoses attached to a CALM buoy in Lazy-S configuration. Six mooring lines are attached to the CALM buoy with a water depth of 100 m in the numerical model. A hydrodynamic model utilising ANSYS AQWA was developed then coupled unto the dynamic model in Orcina's Orcaflex. The studies were carried out to study the effect of flow angles, wave height, soil stiffness and hydrodynamic loads on the structural behaviour of the submarine hoses. Waves at different angles to the submarine hose affected the effective tension more where the hose bends due to the floats attached. Parametric studies were carried out on both linear and nonlinear seabed models, and recommendations were made from the investigations on the submarine hose models.

Keywords: offshore-renewable industry; lazy-s configuration; submarine hose; floating hose; catenary anchor leg mooring (calm) buoy; hydrodynamics; ocean engineering; bonded marine hoses; marine riser; ocean waves; floating offshore platform (fos)

check for updates

Citation: Amaechi, C.V.; Wang, F.; Ye, J. Numerical Assessment on the Dynamic Behaviour of Submarine Hoses Attached to CALM Buoy Configured as Lazy-S under Water Waves. *J. Mar. Sci. Eng.* **2021**, *9*, 1130. http://doi.org/10.3390/jmse9101130

Academic Editors: Rafael Morales and Eva Segura Asensio

Received: 3 September 2021
Accepted: 29 September 2021
Published: 15 October 2021

1. Introduction

Oil exploration has been delivered using more flexible platforms and lighter conduits like composite risers and marine hoses in recent times. With the development of these flexible platforms, there is an increase in energy exploitation developed using offshore systems, such as catenary anchor leg moorings (CALM) buoys, position buoys, wave energy converters (WECs) and ocean observation buoys. However, while some systems are for energy storage and conversion, others are for loading purposes. With variations on environmental conditions for oil explorations, particularly for harsh, hurricane, benign, or squall conditions, there are advances in their application as adopted recently in loading and offloading marine hoses [1–4]. These hoses mainly transfer fluid during production, storage, export, and fluid-service delivery (or simply loading and offloading) purposes [5–7]. These hoses are classified into: floating, submarine, dredging, reeling, and sea-water intake riser (SWIR) hoses. They present the following advantages: they are cost-effective, easier to install, have high flexibility, are mostly self-floating, and are light-weight [8–10]. However, they have a short service life of fewer than 25 years, depending on the application requirement. CALM buoy hose systems can take configurations that differ based on the application and terrain of the environment. The configurations can be Lazy-S, Lazy-wave, Steep-S, or Chinese-Lantern. However, due to different seabed profiles, there are different factors to consider in choosing either linear or nonlinear seabed models. Generally, bonded hoses have extensive applicability in the industry as industrial hoses and marine hoses [11]. However, due to the need for sustainable materials, increased research has been reported on hoses with materials like composites [12–14]. Some advances have been made in using composites as reinforcements on marine hoses [15–19]. Other advances related to the tubular hoses are composite marine risers, which have also notably progressed [20–26]. These structures have been designed by considering different techniques, design tools, and material considerations. As such, there are a variety of methodologies for assessing the structural behaviour and dynamical behaviour of CALM buoy-hose coupled systems [27–30]. The dynamical behaviour of offshore systems attached to a floating offshore platform (FOS) can be investigated using a specialised ocean engineering tool called Orcaflex. Examples are paired-column submersibles (PC Semis) [31–35] and CALM buoys [36–39]. Orcaflex has also found a notable application in pipeline/hoseline strength assessment [40–42] and pipeline installation/laying [43–45].

Currently, applications of offloading hoses connecting the buoy to tankers and loading hoses transferring oil from loading towers have been relatively studied, like in Chinese-lantern and Lazy-S configurations. It is also necessary to consider the effect of different configurations. Figure 1 represents a sketch of a CALM buoy system with submarine hoses attached using Lazy-S configuration under operation. The coupled analysis of CALM buoy has also been studied on elastic seabeds [46–53], but none were reported on the nonlinear seabed. The application of nonlinear seabed profiles has been considered on other offshore structures [54,55]. Examples include nonlinear seabed studies on steel catenary risers (SCR) [56–58]. However, it is crucial to investigate the effect of nonlinear seabed models on CALM buoy systems and on submarine hoses, as this has not been studied.

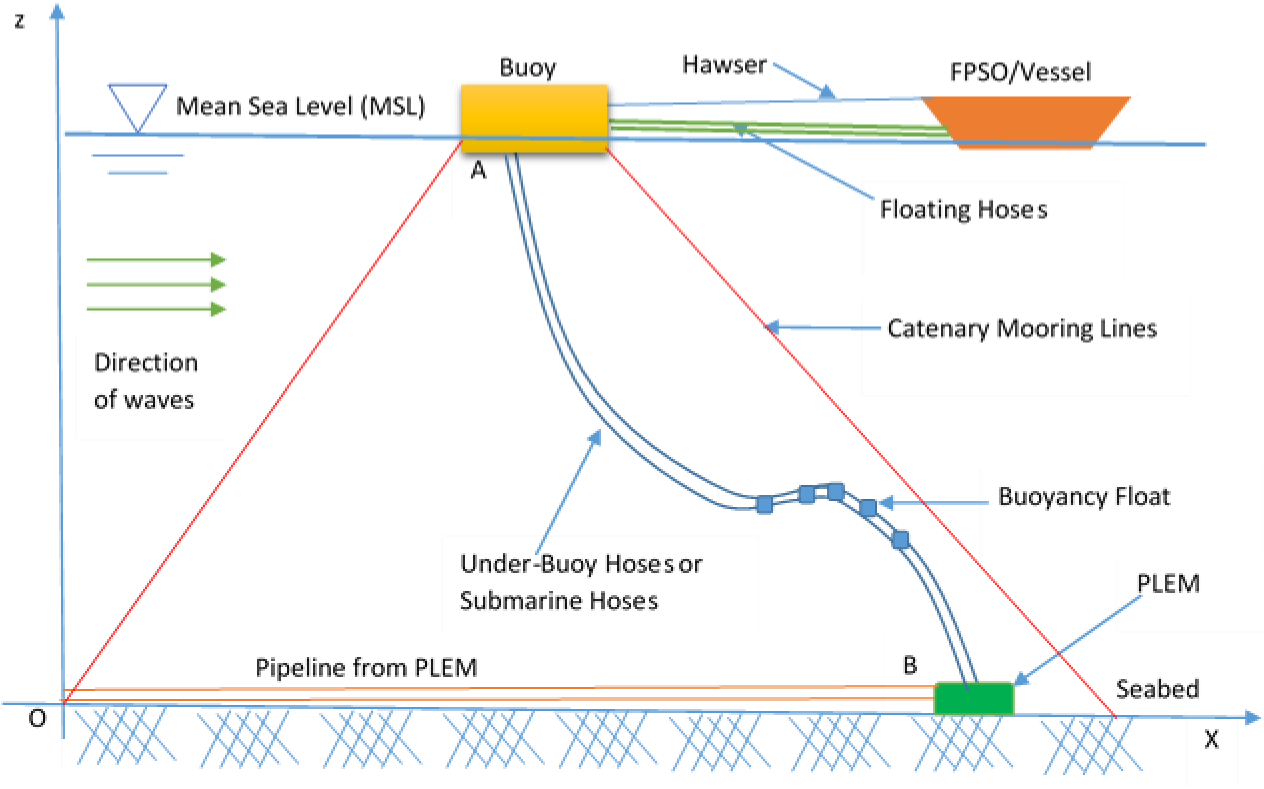

Figure 1. CALM buoy in Lazy-S configuration depicting offloading and loading operation.

Although it has been shown that hoses are affected by the motions of the main CALM buoy [59–63], the effect of the buoy motion on the hose behaviour has not been quantitatively studied. This gap includes hose behaviour relative to the effective tensions, fatigue, full loading history, curvature, and minimum bending radius (MBR) on nonlinear seabeds. A typical field application is the Bluewater's CALM buoy operating in NorthEast African waters located off the shore of Sudan, as shown in Figure 2. In the literature, it has been observed that issues related to offshore hoses include coupling the CALM buoy and the offshore hoses, in addition to the correct determination of the hydrodynamic coefficients. Concerning different operations that are involved in a CALM buoy system, as depicted in Figure 1, it is necessary to understand the dynamical behaviour of the system and how it affects the submarine hose curvature. Challenges with the damping calculation of single point mooring (SPM) systems, led to new techniques like quadratic-absolute-velocity, quadratic-relative-velocity, quadratic-drag-linearization, strength estimation from hydrodynamic loads, and some other formulations using the Morison Equation [64]. Presently, the challenges faced in the industry include providing sustainable hose solutions to meet with the increased demand for hoses with longer service life.

Figure 2. CALM Buoy with an FSO offloading tanker off the shore of Sudan (Courtesy of Bluewater).

Secondly, another challenge reported in the industry is the unexpected rate of marine hose failures due to high curvatures, nonlinearities, control issues, and hose material failure. Some of these failures are from valve malfunction, weak hose couplings, or over tensioned hoses. If marine hoses are tensioned too much as if they are Top Tensioned Risers (TTRs), they could have vey high strains which could lead to material failures. These failures are evidenced in reports on bonded flexible risers failures and marine hose failures [65–69]. However, these hoses satisfy design requirements, but sometimes fail during operation. Thus, recent innovations for controlling marine hoses include hose motion/failure sensors, failure trackers, dual carcass, surge protectors, marine breakaway couplings (MBCs), butterfly valves, hose control systems, and hose end valves (HEVs). Thus, it is necessary to improve the design for the submarine hoses, as well as other factors. In earlier literature ([8,9]), the dynamic amplification factor (DAF) study was presented to help with the problem of submarine hose failures, due to high curvatures. The advantage of DAF is that the maximum dynamic response amplitude can be determined using the static response amplitude without any additional requirement for time history analysis [70–72]. For the hose model, it is also essential to consider the different wave periods, flow angles, soil stiffness, and nonlinearities, like the nonlinear seabed models. The proposed modelling technique will help increase design accuracy and reduce computational time in the design of submarine hoses, particularly on nonlinear seabeds. It will also reduce to submarine hose issues due to wave loads which are not predicted during the design stage.

In this research, the investigations were carried out on CALM buoy coupled with submarine hoses using Lazy-S configuration to look at some parametric effects on the structural performance of hoses resulting from hydrodynamic loads, buoy motion, and the nonlinear seabed model. The model was carried out numerically using different model cases and parameters. The finite element model (FEM) was designed and analysed in Orcaflex 11.0 f using the response amplitude operators (RAO) from ANSYS AQWA 2020 R2. The coupled system and the study validation for the CALM buoy hose model was presented in Section 2. The results from static analysis and dynamic analysis are presented in Section 3, while the parametric studies and discussion are shown in Section 4. Conclusions and recommendations are presented in Section 5.

2. Numerical Model

The numerical analyses were conducted using a coupled analysis. The finite element model (FEM) was developed in the Orcaflex 11.0 f program [73,74]. However, the first design is the hydrodynamic models, developed using ANSYS AQWA 2020 R2 [75,76] to determine the motion behaviour via the response amplitude operators (RAO) [77–79]. The RAOs matrix obtained is then loaded unto the Orcaflex models to carry out dynamic analysis, parametric and sensitivity studies.

2.1. Theory Formulation for Hose Dynamics

2.1.1. Mathematical Formulation of Hose Model

The mathematical formulation for the hose model was developed based on the problem, some simplifications, the author′s experimental cum numerical findings [36–40], and some known offshore engineering practices on submarine hoses [45–47]. The seabed under consideration is horizontal and rigid, and the hose′s material is isotropic and elastic. For this mathematical model, the marine environment is considered as stable for the model. The contact points of the pipeline with the pipe-line end manifold (PLEM) are not considered in the model to keep it simple, but there is tension acting at each hose end. The Cartesian Coordinate System (CCS) is the frame of reference, with an origin as illustrated in Figure 1. The Touch Down Point is the location where the pipeline hits the seabed (TDP). Along the hose string, the model′s natural coordinate system is established. It is also worth noting that the physical parameters of the undersea hose-string are determined by the arc length of the hose string, s.

With consideration on the wave-structure interaction (WSI), the Laplace Equation is applied to formulate the equation governing the motion. This expression is derived from the Continuity Equation for fluids, as represented in Equation (1).

$$\frac{\partial u}{\partial x} + \frac{\partial v}{\partial x} + \frac{\partial w}{\partial x} = 0 \tag{1}$$

The motion of the system can be represented by Equation (2). This equation of motion describes the Newtonian Force, F from the external load of the system as the sum of the inertia force of the system, the viscous damping load, and the elastic force components (also called the stiffness load of the system).

$$F = Ma + Cv + kx \tag{2}$$

For incompressible flow as considered here, the Continuity Equation applies, where u, v and w denote the components of the flow domain.

$$\nabla^2\phi = \frac{\partial^2\phi}{\partial r^2} + \frac{1}{r}\frac{\partial\phi}{\partial r} + \frac{1}{r^2}\frac{\partial^2\phi}{\partial\theta^2} + \frac{\partial^2\phi}{\partial z^2} = 0;\ \ for\ a \le r \le \infty; -h \le z \le \eta; -\pi \le \theta \le \pi \tag{3}$$

For irrotational motion, all the vector components of the rotation are equal to zero.

$$\left(\frac{\partial w}{\partial y}\right)-\left(\frac{\partial v}{\partial z}\right)=0;\left(\frac{\partial u}{\partial z}\right)-\left(\frac{\partial w}{\partial x}\right)=0;\left(\frac{\partial v}{\partial x}\right)-\left(\frac{\partial u}{\partial y}\right)=0 \quad (4)$$

For simplicity, let us denote the vector components in the Cartesian coordinates as $u=\frac{\partial \phi}{\partial x},\ v=\frac{\partial \phi}{\partial y},\ and\ w=\frac{\partial \phi}{\partial z}$, where the scalar function $\varphi(x,y,z)$ are relations used in Equation (4).

Introducing the function ϕ to the Continuity Equation gives the second-order linear differential equation, called the Laplace Transform, given in Equation (5).

$$\nabla^2\phi=\frac{\partial^2\phi}{\partial x^2}+\frac{\partial^2\phi}{\partial y^2}+\frac{\partial^2\phi}{\partial z^2}=0 \quad (5)$$

In the plane coordinate system, the Laplace Equation is given by the relation:

$$\nabla^2\phi=\frac{1}{r}\frac{\partial}{\partial r}\left(r\frac{\partial\phi}{\partial\theta}\right)+\frac{1}{r^2}\frac{\partial^2\phi}{\partial\theta^2}=0 \quad (6)$$

In conventional cylindrical coordinate or polar coordinate (r,θ,z), the Laplace Equation is given by Equation (7):

$$\nabla^2\phi=\frac{\partial^2\phi}{\partial z^2}+\frac{1}{r}\frac{\partial}{\partial r}\left(r\frac{\partial\phi}{\partial\theta}\right)+\frac{1}{r^2}\frac{\partial^2\phi}{\partial\theta^2}=0 \quad (7)$$

For the buoy of radius a, height L, the bounding surface r = a and the two flat parts z = 0 and z = L. Thus, the boundary conditions can be depicted by the following for the given function called the Velocity Potential, $\phi(r,\theta)$:

$$\left.\begin{array}{l}\phi=0;\\ \phi(a,\theta,z);\\ \phi(r,\theta,L)=\phi(r,\theta)\end{array}\right\} \quad (8)$$

2.1.2. Assumptions

As shown in Figure 1, the buoy system consists of a floating buoy, mooring lines, and attached floating hoses and submarine hoses. The buoy is typically treated as a single system, with a rigid body and six degrees of freedom (6DoF). The response of other vessels like the FPSOs, shuttle vessels, or cargo-transport vessels is not considered in this analysis. The following are assumed:

1. The fluid is incompressible, irrotational and bounded by the surface of the buoy, rigid bottom and free surface;
2. The submarine hose is considered as a beam that is under pure bending.
3. The seabed is horizontal and on a rigid plane. For the diffraction analysis, the fluid motion is in cylindrical coordinate system of form (r,θ,z);
4. The influences of both horizontal and shear forces on the curvature are negligible, depending on the bending moment.
5. The internal and external forces will introduce longitudinal forces on the hose. However, the effects can be negligible in depths, having small effects.
6. The hose curvature is the inverse of the minimum bend radius (MBR); and the curvature calculation can be approximated using $\frac{1}{r}=\frac{\partial^2 z}{\partial x^2}$. The measurement of the bend radius of the hose is never less than the MBR;
7. There are some nonlinearities in the motion of fluids within the hose, resulting from some nonlinearities within the hose geometry.
8. A uniform density for the hose is assumed for both the rubber and steel sections.

9. The hose can be made of different sections, flanges, reinforced ends, floated sections, and unfloated sections.
10. The sections of the hose-string can have different section radii.
11. The hose is considered to possess a solidly rigid body with constant bending stiffness for all given cross-sections, transverse to the axis of the hose.
12. The hose also transports (or carries) fluid under high pressure, and the fluid can be oil, gas, or water.

2.1.3. Boundary Condition Formulation

As mentioned in Section 2.1.2, the system's boundary conditions are formulated using some assumptions. Figure 1 depicts the illustrative definition of one (1) floating hose connected between the floating buoy and the FPSO, as well as two (2) undersea hoses connected underneath the buoy in a Lazy-S configuration with the system's environmental pressures, such as waves. The submarine hoses are attached to the bottom by a fixed connection to the pipeline end manifold, and the buoy is cylindrical in shape (PLEM). The seabed is assumed to be horizontal and level. The free floating buoy was used to simplify the modelling of this system. As a result, the mooring lines are ignored in the initial boundary condition formulation. The boundary conditions are formulated using potential theory, shown herein in the above. Equation (1), which is the Laplace transform derived from the continuity equation of fluids, governs the system's motion. Equation (2) is related to the following boundary conditions (represented as a–f), given in Equations (9)–(16):

(a) Dynamic Boundary Conditions:

$$\frac{\partial \phi}{\partial t} + g\eta + \frac{1}{2}\left\{ \left(\frac{\partial \phi}{\partial r}\right)^2 + \left(\frac{1}{r}\frac{\partial \phi}{\partial \theta}\right)^2 + \left(\frac{\partial \phi}{\partial z}\right)^2 \right\} = 0;\ for\ r \geq a;\ z = \eta(x, y, t) \tag{9}$$

(b) Kinematic Boundary Conditions:

$$\frac{\partial \eta}{\partial t} + \left(\frac{\partial \phi}{\partial r}\right)\left(\frac{\partial \eta}{\partial r}\right) + \frac{1}{r^2}\left\{ \left(\frac{\partial \phi}{\partial \theta}\right)\left(\frac{\partial \eta}{\partial \theta}\right) \right\} = \frac{\partial \phi}{\partial z};\ for\ r \geq a;\ z = \eta(x, y, t) \tag{10}$$

(c) Free Surface Boundary Conditions:

$$z = \eta(x, y, t) \tag{11}$$

$z = \eta(x, y, t)$ represents the free surface [80]. The free surface boundary conditions are given in Equations (6)–(7), which are to be satisfied by both the wave elevation η and velocity potential ϕ.

(d) Body Surface Boundary Conditions:

$$\frac{\partial \phi}{\partial r} = 0;\ for\ r = a; -h \leq z \leq \eta \tag{12}$$

(e) Seabed (or bottom) Boundary Conditions:

For an impermeable seabed of depth h (x, y), carrying a floating buoy, the seabed boundary condition is given by Equation (13);

$$\frac{\partial \phi}{\partial z} = 0;\ for\ z = -h \tag{13}$$

(f) Radiation Boundary Conditions:

Assuming at infinity, the radiation boundary condition is given by Equation (9), where ϕ_S denotes the scattered wave potential for this condition and ϕ_I denotes the incident wave potential.

$$\phi(r,\theta,z,t) = Re\Big[\phi(r,\theta,z)e^{i\sigma t}\Big]= Re\big[(\phi_I + \phi_S)e^{i\sigma t}\Big] \tag{14}$$

Thus, Equations (15)–(16) will satisfy the radiation potential at infinity;

$$\lim_{kr\to\infty} \sqrt{kr}\left(\left(\frac{\partial}{\partial r}\right) \pm ik\right) = 0;\ i = \sqrt{-1} \tag{15}$$

$$\lim_{kr\to\infty} \sqrt{kr}\left(\left(\frac{\partial}{\partial r}\right) \pm ik\right)(\phi\ - \phi_I) = 0;\ i = \sqrt{-1} \tag{16}$$

2.1.4. Hose Bending and Lateral Deflection

In the case of the end (or terminus) at point A in Figure 3a, the distance is $x = 0$. There is an asymptotic connection as the submarine hose-strings move due towards responses from wave and vibration motions. Equation (17), which predicts the movement at the hose-string′s end, provides this information. Thus:

$$u(x = 0) = \cos\sigma t \tag{17}$$

where a_h is the amplitude of the buoy motion, σ is the circular frequency of the wave, k is the wave number, and ω is the angular frequency. This equation is only real, when there is a steady harmonic motion that is relative to the configuration that can be represented straight and lateral to the buoy when it is positioned deeply backwards. Thus,

$$u(x = 0) = (1 - \cos\sigma t) \tag{18}$$

Consider a beam model with a force and moment element with longitudinal displacement u and lateral displacement w, as shown in Figure 3. The equations of motion in the x-direction and z-direction can be expressed in the form given in Equation (19).

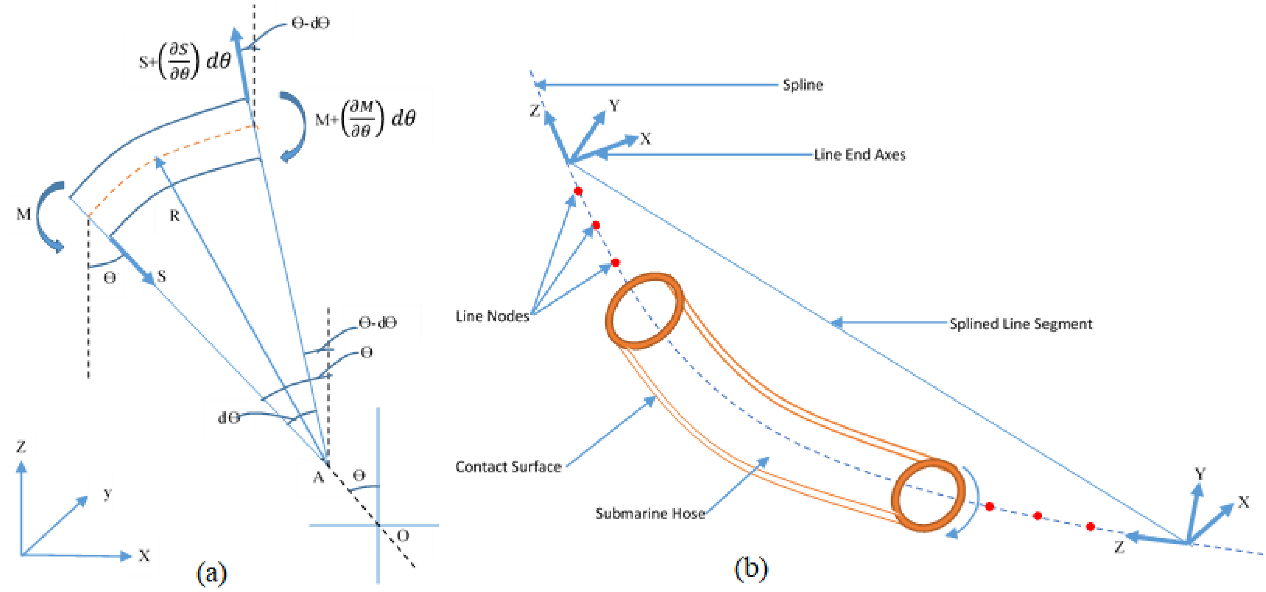

Figure 3. An illustration showing (**a**) displaced hose-beam element showing moments and forces, and (**b**) Submarine hose segment showing spline line and nodes.

Along the x-direction, the equation of motion is:

$$S\theta - \left[S + \left(\frac{\partial S}{\partial \theta}\right) d\theta\right](\theta - d\theta) = mRd\theta \frac{\partial^2 u}{\partial t^2} \tag{19}$$

Diving both sides by $d\theta$, and simplifying gives:

$$S - \left(\frac{\partial S(\theta + d\theta)}{\partial \theta}\right) = mR\frac{\partial^2 u}{\partial t^2} \tag{20}$$

Along the z-direction, the equation of motion is:

$$-S + \left[S + \left(\frac{\partial S}{\partial \theta}\right) d\theta\right] = mRd\theta \frac{\partial^2 w}{\partial t^2} \tag{21}$$

Diving both sides by $d\theta$, and simplifying gives:

$$\left(\frac{\partial S}{\partial \theta}\right) = mR\frac{\partial^2 u}{\partial t^2} \tag{22}$$

Taking moments about the edge of the elements in LHS:

$$M - +Rd\theta = 0 \tag{23}$$

By dividing both sides by $d\theta$, and simplifying gives:

$$-\left[\left(\frac{\partial M}{\partial \theta}\right)\right] + SR + \left[\left(\frac{\partial S}{\partial \theta}\right)d\theta\right] = 0 \tag{24}$$

As δS limits to 0, gives:

$$\frac{\partial M}{\partial \theta} = SR \tag{25}$$

Applying Beam Bending Theory, gives:

$$\frac{M}{EI} = \frac{1}{R} = -\frac{\partial^2 z}{\partial x^2} \tag{26}$$

Applying the hose modelling method by O'Donoghue ([81–84]) by assuming that $\theta = \frac{\partial z}{\partial x}$, $Rd\theta = dx$, and w = z; and applying these into Equations (25) and (26), the equation of motion along the longitudinal or x-direction, yields Equation (27) and the lateral or y-direction in Equation (28):

$$EI\,\frac{\partial}{\partial x}\left(\frac{\partial^3 z}{\partial x^3}\cdot\frac{\partial z}{\partial x}\right) = m\frac{\partial^2 u}{\partial t^2} \tag{27}$$

$$EI\,\frac{\partial^4 y}{\partial x^4} + m\frac{\partial^2 y}{\partial t^2} = 0 \tag{28}$$

For the lateral deflection $z(x,t)$ along the length of the beam section, Equation (28) yields the equation of motion for beam bending. Equation (27) depicts the longitudinal motion of the beam with the point of force applied exclusively at $x = 0$, which is the position on the beam model representing the inertial end condition of free lateral vibration. Detailed dynamic modelling states of the hoses are in [6]. For further studies on the mathematical modelling approach for the hose model, see literature on different marine hose studies by Amaechi ([6–9,26]), O'Donoghue ([81–84]), and Brown ([85–87]).

2.1.5. Boundary Element Method (BEM)

The use of Morison′s equation in the analysis of waves on the CALM buoy is crucial for determining the motion behaviour. As shown in Equations (29)–(30), these wave forces are a direct function of the fluid phase pressure 'P_θ' exerted on the body.

$$P_\theta \ \frac{H}{2}\left(P_r\cos\theta + P_i\cos\theta\right) \tag{29}$$

where the subscripts r and i respectively denote the real and imaginary components of the pressure, H denotes the wave height and θ denotes the flow angle.

$$F_i = \iint\limits_{s_w} P_\theta n_j \mathrm{d}S = -\rho \iint\limits_{s_w} (j\omega\phi + gz)n_j \ \mathrm{d}S \tag{30}$$

F_i is the first order pressure force, s_w is the wetted surface, n_j is the normal component of the wetted surface vibration mode, z is the height of the submerged hull length, ω angular velocity, g is gravity, ρ fluid density, ϕ wave complex potential which can be written as:

$$\phi = \phi_i + \phi_s + \sum\nolimits_{j=1}^{6} \phi_r \tag{31}$$

where the terms ϕ_i, ϕ_s and ϕ_r are the incidence, scattered and radiation wave potentials respectively, and j denotes the mode of vibration of the body.

The Navier–Stokes equation can be employed for incompressible fluid operating in irrotational motion under a sea depth h, on a floating buoy of depth d, whereby the wave theory used to determine the potential relationship in Equation (31) is taken into account. The velocity potential is written as:

$$\phi(x,y,t,z) = \varphi(x,y)f(z)e^{i\omega t} \tag{32}$$

Considering Equation (5), used in formulating the boundary conditions for which is the Laplace transform derived are formulated using potential theory, thus the fluid potential is:

$$\nabla^2\phi = 0 \tag{33}$$

According to diffraction theory, there will be no normal flux or normal velocity for impermeable scenarios, as shown in Equation (34), reducing the problem to a two-dimensional problem with respect to the velocity potential $\phi(x,y)$ as:

$$\nabla\phi\cdot\vec{n} = \frac{\partial\varphi}{\partial n} = 0 \tag{34}$$

Despite the force on the submarine hose element in Figure 3b, F can be derived utilising Cartesian coordinates (x,y,z) or polar coordinates (r,θ,z). Thus, the total force can be expressed as a function of the pressure of the fluid, the sea depth and the angle made by the hose element. Therefore, we have:

$$\vec{F} = -P\cos\theta dS; -P\sin\theta dS \tag{35}$$

$$\vec{F} = -\int_S P\vec{r}\,dS \tag{36}$$

$$\vec{F} = -\int_0^{2\pi}\int_{-d}^{0} P\vec{r}.rd\theta dS \tag{37}$$

Based on a sea depth, z, the force per unit length at the depth where the surface of the buoy element is S,

$$\vec{F} = -\int_0^{2\pi} P\vec{r}.rd\theta \tag{38}$$

2.1.6. Hydrodynamic Equations

In previous research ([6,8]), the hydrodynamic force acting on a body in the horizontal plane, may be mathematically stated as Equation (39);

$$\left\{\mathrm{F_{hyd}}\right\} = [\mathrm{M}]\{\ddot{x}\} + [\mathrm{C}]\{\dot{x}\} + [\mathrm{M}]\{x\} \tag{39}$$

where $\{x\}$ denotes the motion vector, [K] denotes the stiffness matrix, [C] denotes the structural damping matrix, [M] denotes mass matrix of the hull while $\{\mathrm{F_{hyd}}\}$ denotes the hydrodynamic force vector.

The wave exciting force was derived from the hydrodynamic exciting forces, since they are a product of the wave potential, which is a function of incident waves for each unit amplitude. The wave exciting forces can be expressed as Equation (40),

$$\{F_i^w\} = -\rho \iint (if_w - \{W\}\cdot \nabla)\left(u_i + u_d\right)e^{-if_w t}\mathrm{n_i}\ \mathrm{ds} \tag{40}$$

where $\{W\}$ denotes the velocity field vector of the steady flow; f_w denotes the wave oscillating frequency, u_i denotes the incident diffraction wave potentials per unit amplitude; u_i denotes the diffraction wave potentials per unit amplitude; ρ denotes the density of sea water; and i denotes degree of freedom (DoF).

2.2. *Hydrodynamic Model*

The design consideration for the floating CALM buoy is for operation in 100 m water depth. The model is established by using ANSYS AQWA 2020 R2 [8,75,76], where diffraction/radiation method is applied in solving the 3-dimensional problems of the floating CALM buoy. The adopted wave spectrum is the JONSWAP (Joint North Sea Wave Project) wave spectrum in the numerical analysis. The boundary box for the sea area utilised for the numerical model in ANSYS AQWA 2020 R2 is 150 m by 150 m. The hydrodynamic panel approach was used in the diffraction analysis, as shown in Figure 4a, depicting the ocean-view buoy model, with the wave direction on the buoy. The buoy's skirt was designed as solid with a smaller diameter to accurately reflect its effective zone, which is detailed in Table 1. The ocean (or environmental) conditions used for the study, including the waves, depicted in Figure 4b, are carried out according to industry standards [88–91]. The hydrodynamic components are presented in Section 2.5, with details in [8,9].

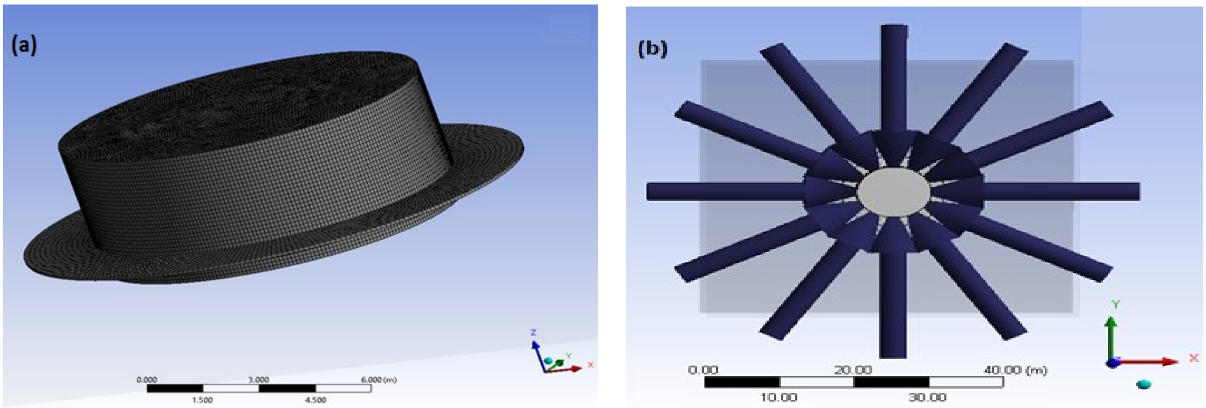

Figure 4. Buoy Design in ANSYS AQWA 2020 R2 showing (**a**) Hydrodynamic Panel, and (**b**) Wave Direction on buoy.

2.2.1. Buoy Design

The details of the particulars for the buoy utilised in the numerical modelling model are given in Table 1. The model was designed using 6D buoys in Orcaflex, and in ANSYS AQWA. To ensure that buoyancy effect is considered, the draft size of 2.4 m was considered. Figure 5 shows two 3D views of the CALM buoy in Orcaflex-shaded and wireframe.

Table 1. Parameters for the Buoy.

Particulars	Value
Buoy Height (m)	4.40
Draft size (m)	2.40
Water Depth (m)	100.00
Buoy Mass (kg)	198,762.00
Main body diameter (m)	10.00
Skirt diameter (m)	13.87

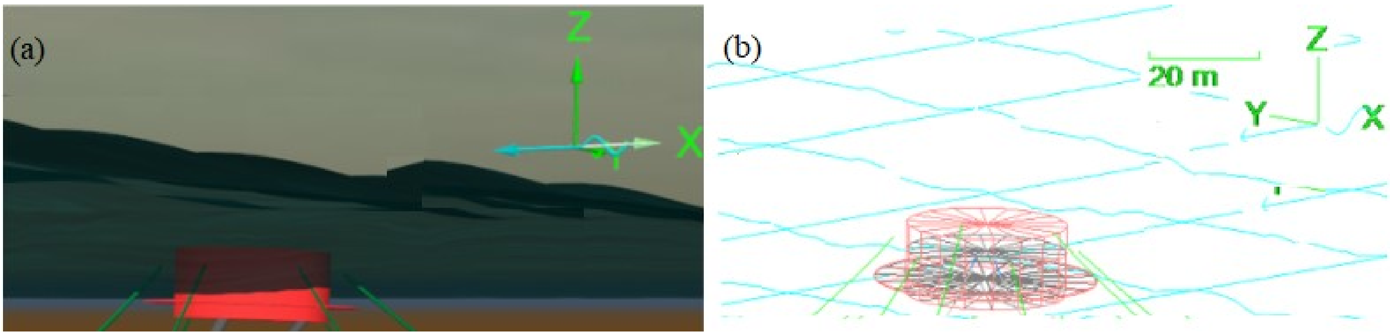

Figure 5. CALM Buoy Model showing (**a**) shaded view, and (**b**) wireframe view, modelled in Orcaflex 11.

2.2.2. Submarine Hoses

The submarine hoses are in Lazy-S configuration, as illustrated in Figures 1 and 6, was designed for 1900 KN/m^2 (19 bar) pressure application. Two submarine hose strings are connected to the base of the buoy at the top and the pipeline end manifolds (PLEMs) at the bottom. Each of the submarine hoses is 162.065 m lengthwise, consisting of 43 sections and 525 segments, as presented in Table 2. In the model, there are 21 hose sections in the each hose-string—Hose1 and Hose2. They are compartmented into 3 groups—the far-end (Group-Section 1), the mid-sections (Group-Sections 2–20) and the near-end (Group-Section 3). Both the far end and the rear ends have reinforced hose ends. The fluid contents inside, the internal pressure, the self-weight, the buoyancy and the weight of the floats are considered. A uniform contents method was applied to model the fluid contents of the hose, which is crude oil with a density of 821 kg/m^3. Fully filled conditions are assumed with 0 kPa inner pressure of the fluid in the hose. The Orcaflex 3D view of the CALM buoy Lazy-S model, showing the ocean environment, is presented in Figure 7a. The section profile for the submarine hose in Orcaflex 11.0f is depicted in Figure 7b. The outer and inner diameters of the hoses are 0.650 m and 0.490 m, respectively. The model for the submarine hose has already been validated in some research studies [8,9].

Table 2. Submarine Hose Arrangement with section details.

Section Number	Sub-Sections	Particulars	Inner Diameter (m)	Outer Diameter (m)	Section Length (m)	Segment Length (m)	Number of Segments	Unit Mass (kg/m)	Volume (m^3)	Segment Weight (N)
Hose Group 1—Section 1	1	Fitting	0.489	0.650	1.0	0.800	1	495	0.330	492.5
	2	Reinforced Hose End	0.489	0.650	0.2	3.000	15	239	1.002	721.5
	3	Hose Body	0.489	0.650	0.5	3.236	6	180	1.074	582.5
	4	Hose End	0.489	0.675	0.5	0.895	2	200	0.320	179.0
	5	Fitting	0.489	0.650	1.0	0.800	1	495	0.330	492.5
Hose Group 2—Section 2—Section 20 (same)	6	Fitting	0.489	0.650	1.0	0.800	1	495	0.330	492.5
	7	Hose End	0.489	0.675	0.5	0.895	2	200	0.320	179.0
	8	Hose Body	0.489	0.650	0.2	3.840	19	180	1.274	691.2
	9	Hose End	0.489	0.675	0.5	0.895	2	200	0.320	179.0
	10	Fitting	0.489	0.650	1.0	0.800	1	495	0.330	492.5
Hose Group 3—Section 21	11	Fitting	0.489	0.650	1.0	0.800	1	495	0.330	492.5
	12	Hose End	0.489	0.675	0.5	0.895	2	200	0.320	179.0
	13	Hose Body	0.489	0.650	0.5	3.236	6	180	1.074	582.5
	14	Reinforced Hose End	0.489	0.670	0.2	3.000	15	240	1.064	724.6
	15	Fitting	0.489	0.650	1.0	0.800	1	495	0.330	492.5

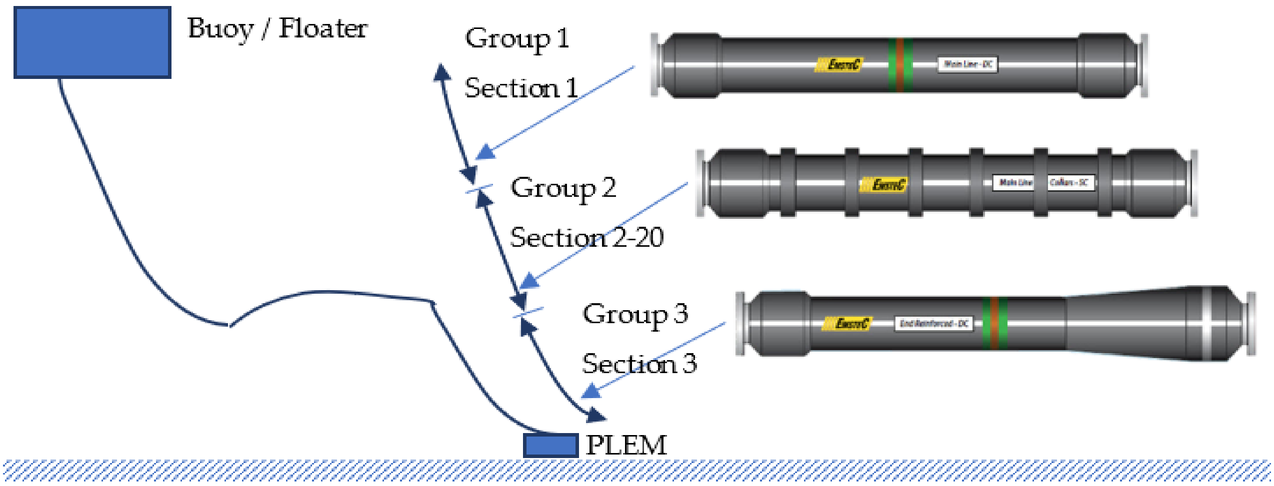

Figure 6. Schematic of marine hoses attached to a floating buoy in Lazy-S config. (Author, but Hose Courtesy: EMSTEC).

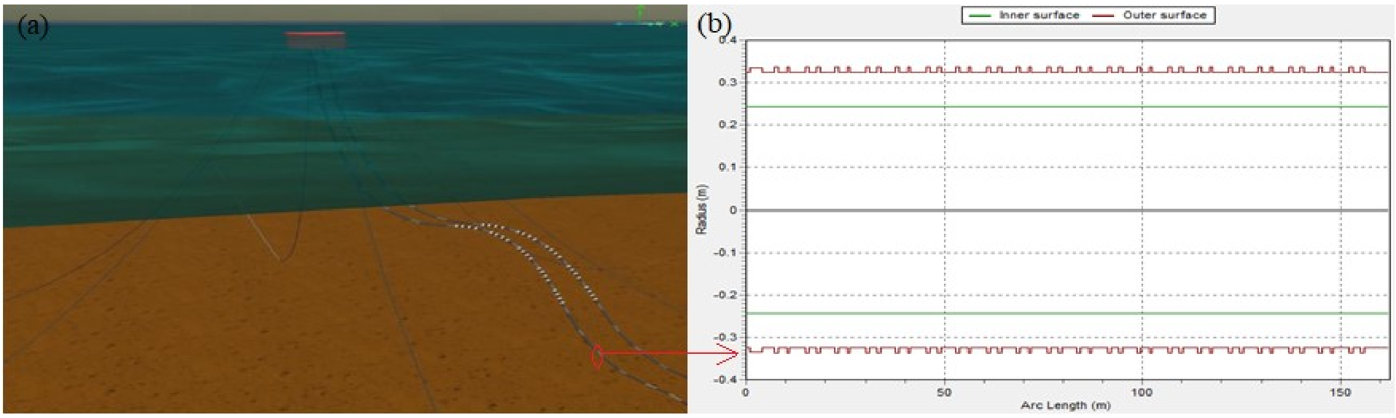

Figure 7. Numerical hose model in Orcaflex 11.0 f showing (**a**) CALM Buoy Lazy-S configuration showing mooring lines and submarine hoses, and (**b**) Submarine Hose Profile showing the radii for inner and outer surfaces.

2.2.3. Mooring Lines

The mooring arrangement is made up of six mooring lines located along the circumferential direction, which are modelled. The mooring lines have the same stiffness and are connected as catenary mooring lines. The mooring lines are 60 degrees apart, as detailed in Table 3. Each mooring line is made up of two sections of steel chains. One end of the mooring line is attached to the cylindrical buoy, while the other end is anchored to the seabed, as presented in Figures 7a and 8a,b.

Table 3. Mooring Lines Parameters.

Parameters	Value
Poisson Ratio	0.5
Nominal Diameter (m)	0.120
Ratio of Section Lengths	150:195
Mass per unit length (kg/m)	0.088
Coefficient of Drag, C_d	1.0
Coefficient of Mass, C_m	1.0
Bending Stiffness (N*m^2)	0.010
Axial Stiffness, EA (kN)	407,257
Contact Diameter (m)	0.229

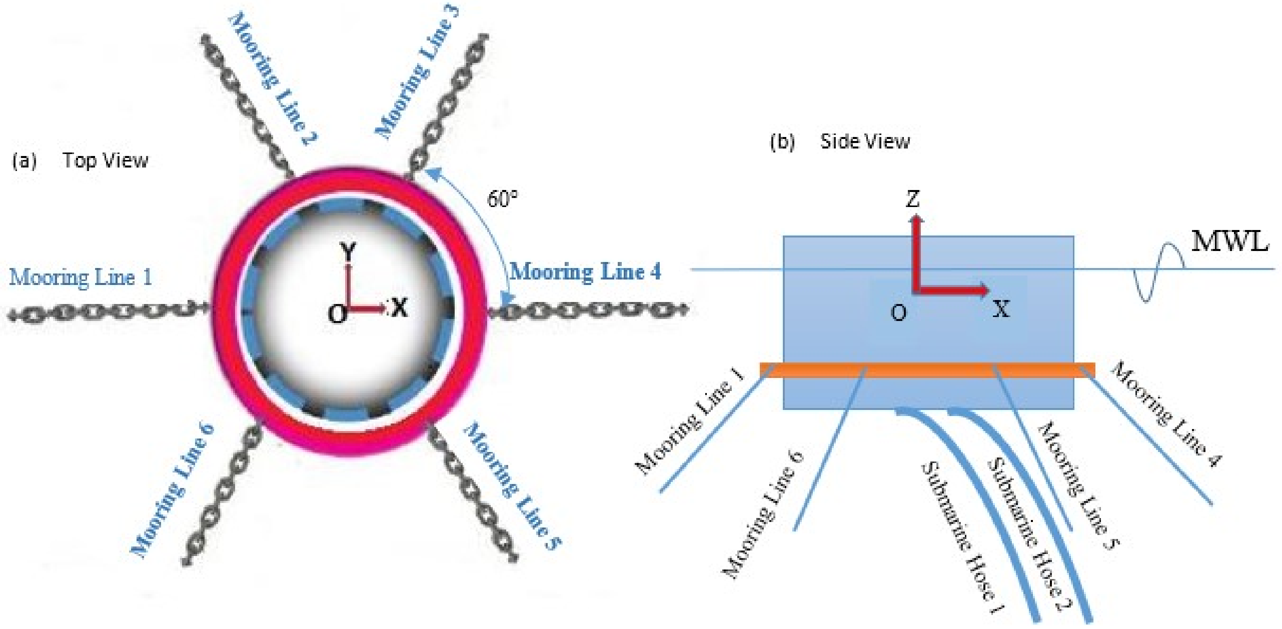

Figure 8. The Cartesian Coordinate System showing the Buoy and Mooring Lines in (**a**) top view (**b**) side view.

2.2.4. Buoyancy Float

With a float incorporated as part of the hose line, the buoyancy connexions on the hoses were designed. The design of the float materials is constructed as shown in Table 4, in accordance with the OCIMF industry requirements [92–94]. The buoyancy of the submarine hose line is obtained by designing a series of floats added together, as shown in Figures 7a and 9.

Table 4. Parameters of Buoyancy float.

Parameters	Value
Pitch of Floats, P_f (m)	2.00 (depends on section)
Weight in Air (kg)	102.00
Outer Diameter (m)	1.23
Net Buoyancy (kg)	280.00
Inner Diameter, D_f (m)	0.799
Length of Float, L_f (m)	0.60
Design Depth (m)	40
Material for Shell	Polyethylene
Material for Filling	Polyurethane foam
Material for Metallic Sections	Stainless Steel
Float Classification	Standard bolted-type float

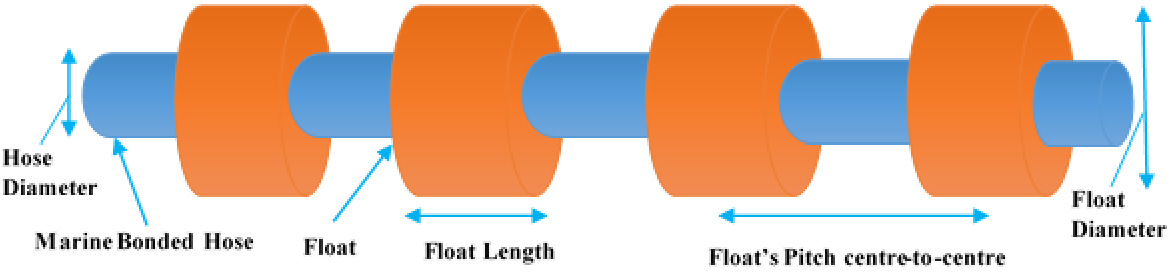

Figure 9. Typical floats attached to offshore submarine hoses.

2.3. Finite Element Model (FEM)

Orcaflex is used for the FEM which applies line theory, where lumped mass model is used for mooring lines, as shown in Figure 10a,b. Details on the principle of line theory used in the FEM of the submarine hose lines and the mooring lines in Orcaflex are reported in [75,76]. For submarine hoses, it applies lines, which are considered as massless with distributed concentrated mass. In the Orcaflex model, 43 segments were used to model the submarine hose lines, as detailed in Section 2.2.2. The hydrodynamic properties of the CALM Buoy were coupled into the Orcaflex model. Every node is a short straight rod on either side of the node that represents two half-segments, as shown in Figure 10c, except for the end-nodes with one half-segment. At these nodes, moments and forces were applied, while weights were applied at offsets. An axial spring and a damper at the middle of the line segment are formulated on the axial stiffness and damping of the hose-line, applying opposite and equal effective tension forces to the nodes on each end of the line segment. Rotational springs and dampers on either side of the node, stretching between the node′s axial direction N_z and the line segment′s axial direction S_z, depict the bending properties. A torsional spring also models the torsional stiffness and damping with a damper at the middle of the line segment. An opposite and equal torque moment is applied at that node of the torsional spring-damper.

Analytically, there are different hose-riser formulations, based on the vibration of thick beams, using Euler or Timoshenko beam theory [95–97]. Numerical models were used to validate this FEM model, shown in Figure 11. The mooring lines were calculated using catenary method in the statics mode, using catenary equation [98–103]. Results of bending moments and effective tension were obtained. Effective tension is the sum of the moments at a depth in a tube. It is called tension only for convenience. it tells the user how to account for the pressure in the fluid inside and outside of the pipe. OrcaFlex identifies two types of tension, namely: the wall tension, T_w and the effective tension, T_e, related by the Equation (41), where p_i is internal pressure, p_o is external pressure, a_i= internal cross section area, and a_o= external cross section area.

$$T_w = T_e + (p_i \cdot a_i - p_o \cdot a_o) \tag{41}$$

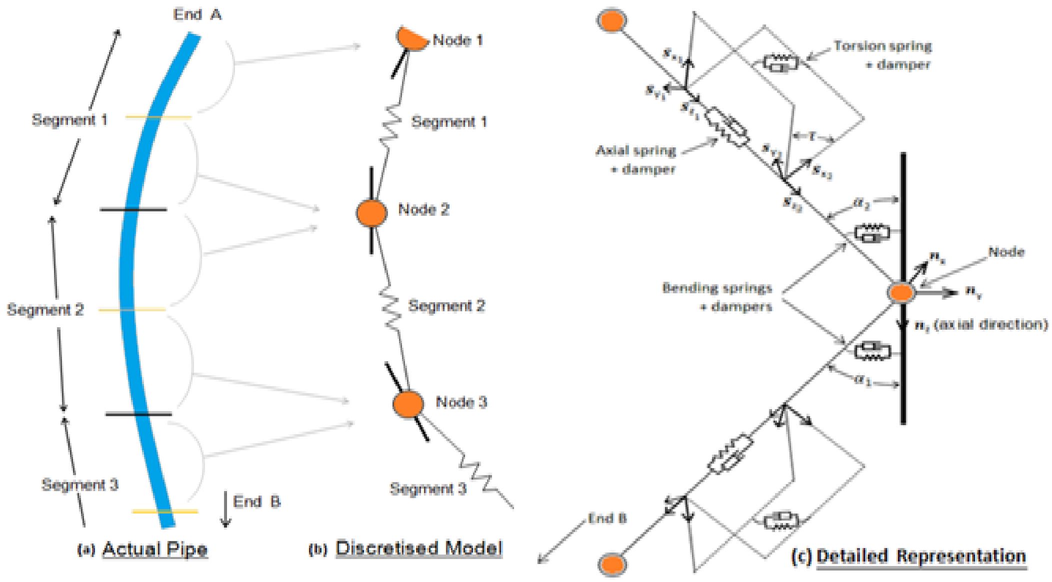

Figure 10. Orcaflex Line Model showing (**a**) the main line, (**b**) the discretized model, (**c**) Detailed model representation with 3 spring-damper types (Adapted, courtesy of Orcina [73]).

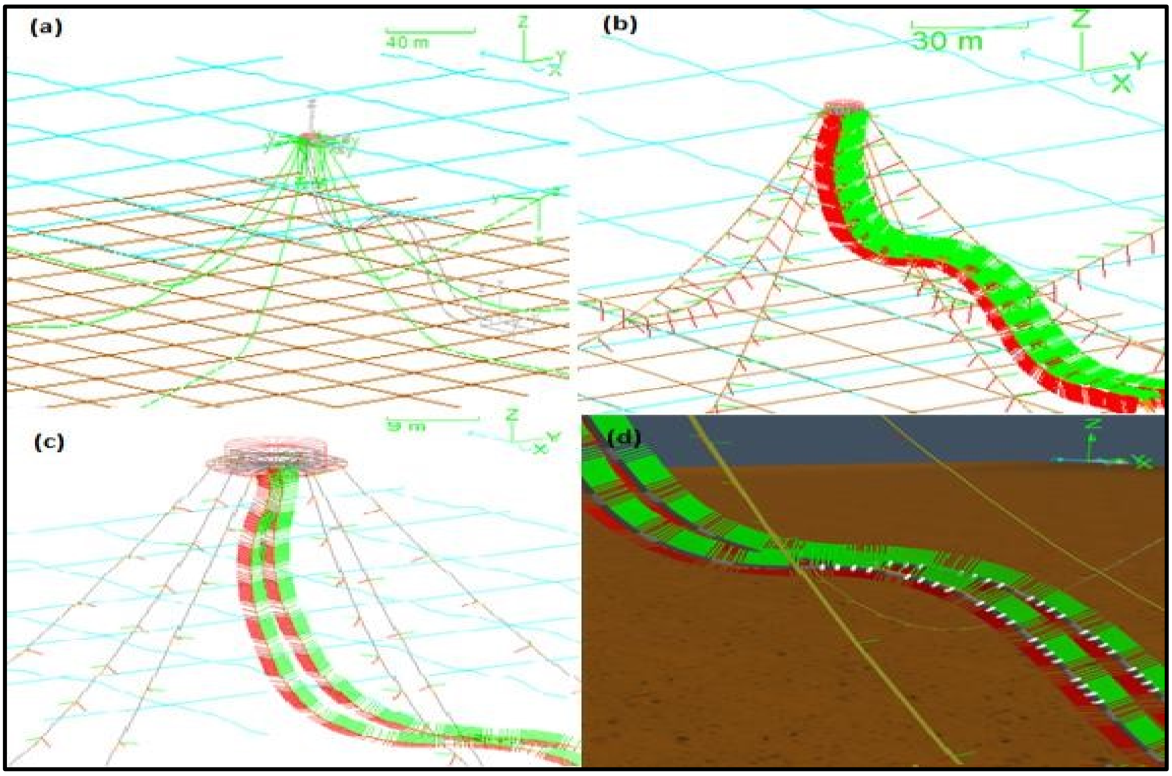

Figure 11. CALM Buoy system finite element model showing Orcaflex details of (**a**) FEM wireframe view (**b**) nodal axes (**c**) buoy and mooring line nodes (**d**) submarine hoses with floats.

2.4. Seabed Model

The seabed profile is modelled as a 3D seabed, and it is determined by using the top surface of the seabed with respect to the sea surface, as shown in Figures 7a and 11. The seabed origin in the X-Y coordinate is taken from the origin. In this study, two seabed models were comparatively considered—the elastic and the nonlinear seabed models. The parameters for the nonlinear soil model are presented in Table 5, while the parameters for the seabed and ocean conditions are presented in Table 6. The seabed model considered is the non-linear seabed theory in Orcaflex, as illustrated in Figure 12. The elastic (or linear) model is simply acting on the elastic seafloor. In directions normal and tangential to the seafloor plane, it functions as a basic elastic spring. The stiffness in the normal direction can be determined independently of the tangential directions′ stiffness. Normal stiffness can be either linear or nonlinear, but tangential stiffness is always linear. Conversely, the nonlinear soil model is an advanced version of the normal-direction seabed resistance model. It covers the modelling of suction effects when a penetrating object rises up, as well as the nonlinear hysteretic behaviour of bottom soil in the normal direction. Tangential stiffness is also linear, as in the elastic model.

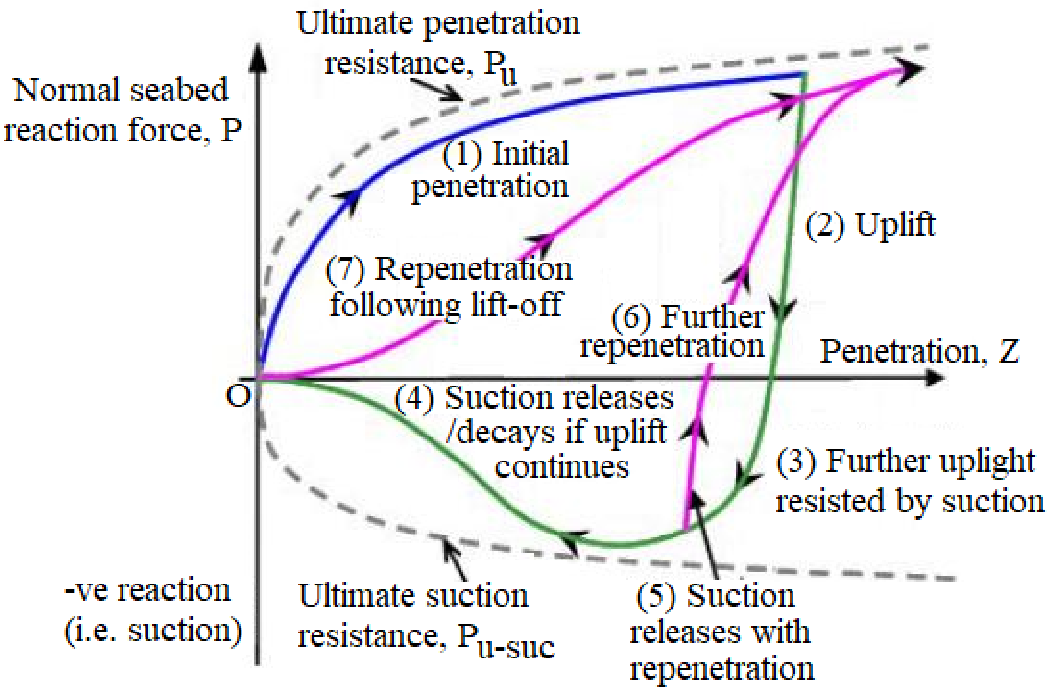

Figure 12. Soil model characteristics showing different modes (Adapted, courtesy of Orcina [73]).

The resistance to penetration on a nonlinear seabed model increases as penetration and decreases as uplift. This representation shows the initial, uplift and repenetration modes for the nonlinear seabed model, which has been validated with details in the literature. Seabed damping is the constant of proportionality of the damping force, and is a percentage of critical damping. Seabed damping is always zero when using the implicit integration scheme [54,73,74].

For the model characteristics, the uplift and repenetration modes are not employed in the static analysis. At initialization, the penetration mode is switched to initial penetration if the penetration is positive, or not in contact if not. As a result, the static position determined is based on the premise that any static penetration occurred as a single progressive penetration. This mode does not account for any uplift or repenetration that may have occurred during the first installation. Unlike OrcaLay, OrcaFlex is limited here, as it cannot process such effects, because it just has a limited understanding of the instance when the line was originally laid, and a few initial positions. However, Orcaflex still produces a well-validated seabed model.

The penetrator commences the dynamic simulation in either not-in-contact mode or initial penetration mode, based on the results of the static analysis. If it starts in non-contact mode, it switches to first penetration mode when the penetration becomes positive for the first time. After initial penetration in the dynamic simulation, the penetrator remains in initial penetration mode until it begins to lift up, at which point, it switches to uplift mode. The penetrator then remains in uplift mode until the penetration drops to zero, at which point, it breaks contact and switches to not in contact mode, or until the penetration increases again, at which point, it switches to repenetration mode. Repenetration mode lasts until the penetrator begins to rise up again, at which point, it switches to uplift mode. If the penetrator remains in touch with the seafloor but oscillates up and down, the uplift and repenetration modes are switched back and forth. Note that repenetration mode, not initial penetration mode, is entered when the penetrator breaks contact and then makes contact again. The assumption is that the second and subsequent intervals of contact are contacting the same area of the seabed that was disrupted by the initial penetration.

The shear strength is determined by the undrained shear strength gradient, ρ, and the undrained shear strength at mudline, s_{u0}. The undrained shear strength at any given penetration distance z is then:

$$s_u(z) = s_{u0} + \rho z \tag{42}$$

Under the elastic seabed model, the seabed behaves as an elastic spring in the normal direction, with spring strength determined by the normal seabed stiffness parameter. The normal stiffness reaction force, $\mathbf{f}_R$ is represented by Equation (43):

$$\mathbf{f}_R = r(d)\, a\, (\mathbf{n}) \tag{43}$$

where d depicts depth of penetration, r(d) depicts reaction force per unit contact area at penetration depth, n depicts the unit vector in the outward normal direction to the seabed, and a depicts contact area for the buoy or line.

According to Orcina ([73,74]), the resistance formulae may be expressed so that as the penetration z decreases (for uplift) or increases (for penetration), then the resistance asymptotically approaches the ultimate suction resistance $P_{u\text{-}suc}(z)$ (for uplift) or the ultimate penetration resistance $P_u(z)$ (for penetration). These ultimate penetration and suction asymptotic limits are represented by:

$$P_u(z) = N_c(z/D)\, s_u(z)\, D \tag{44}$$

$$P_{u\text{-}suc}(z) = -f_{suc}\, P_u(z) \tag{45}$$

where D denotes penetrator contact diameter, $N_c(z/D)$ denotes bearing factor; f_{suc} denotes non-dimensional suction resistance ratio parameter, and $s_u(z)$ denotes the undrained shear strength at penetration z.

The starting penetration and resistance values, z0 and P0, are both zero. The penetration resistance is then given by:

$$P(z) = H_{IP}(\zeta)\, P_u(z) \tag{46}$$

where $H_{IP}(\zeta) = \zeta/(1 + \zeta)$. The term $H_{IP}(\zeta)$ is a hyperbolic factor that takes the value 0 when $\zeta = 0$ (when initial penetration starts), 0.5 when $\zeta = 1$, i.e., when z = D/Kmax, and asymptotically approaches 1 as penetration becomes large compared to D/Kmax ([73,74]). Similarly, the term $H_{RP}(\zeta - \zeta 0)$ in Equation (47) is a hyperbolic factor that has the value 0 when $\zeta = \zeta 0$ at the start of this repenetration, and asymptotically approaches 1 if the non-dimensional repenetration $\zeta - \zeta 0$ becomes large. Moreover, the term $H_{UL}(\zeta 0 - \zeta)$ is a hyperbolic factor that is 0 when $\zeta = \zeta 0$ at the start of this uplift, and asymptotically approaches 1 if the non-dimensional uplift $\zeta 0 - \zeta$ becomes large ([54,73,74]).

The penetration resistance during repenetration mode is expressed as Equation (47), while during uplift mode, is expressed as Equation (48):

$$P(z) = P_0 + H_{RP}(\zeta - \zeta 0)\ (P_u(z) - P_0) \tag{47}$$

$$P(z) = P_0 - H_{UL}(\zeta 0 - \zeta)\ (P_0 - P_{u\text{-}suc}(z)) \tag{48}$$

Table 5. Non-linear Soil Model parameters.

Parameter	Symbol	Value
Mudline Shear Strength (kPa)	S_{u0}	4.5
Shear Strength Gradient (kPa/m)	S_g	1.5
Saturated Soil Density (te/m^3)	ρ_{soil}	1.5
Power Law Parameter	a	6.0
Power Law Parameter	b	0.25
Soil Buoyancy Factor	f_b	1.5
Normalized Maximum Stiffness (kNm^{-1}m^2)	K_{max}	200.0
Suction Resistance Ratio	f_{suc}	0.7
Suction Decay Parameter	λ_{suc}	1.0
Repenetration Parameter	λ_{rep}	0.3

Table 6. Seabed and Ocean Parameters.

Parameter	Value	Parameter	Value
Water Density (kgm^{-3})	1,025	Ocean Temperature (°C)	10
Ocean Kinematic Viscosity (m^{2}s^{-1})	1.35×10^{-6}	Water Depth (m)	100.0
Wave Amplitude (m)	0.145	Seabed Friction Coefficient	0.5
Seabed Stiffness (kNm^{-1}m^2)	7.5	Seabed Shape Direction (°)	0
Seabed Critical Damping (%)	0	Seabed Model Profile Type	3D Profile Nonlinear

2.5. Hydrodynamic Components

2.5.1. Environmental Conditions

This study employs three combinations of environmental conditions. In this study, the linear theory with respect to the spectral components is used in the simulation of the sea state. The simulations are run for irregular waves in "fully developed sea conditions", for the duration of three (3) hours. For a fully developed sea (fds), the amount of energy given by the wind equals the amount of energy lost in breaking waves, as illustrated in Figure 13. Theoretically, the sea is said to have completely formed when the wind has supplied its greatest energy to the waves. At this point, regardless of duration, the maximum ocean waves or sea condition is produced by a given wind force blowing over adequate fetch. The fetch will have created the maximum frequency range for that wind, and this maximum frequency range will be present near the fetch′s leeward edge. No frequency lower than the minimum frequency value for the wind speed in consideration is created once the sea has fully developed, regardless of the duration for which the wind blows for. In a nutshell, the waves cannot get any bigger than the wind speed′s maximum value. The area along the windward edge is said to be in a constant condition when the sea has fully evolved, because the frequency range does not expand any more. The primary portion of the fetch reaches the steady state if the wind continues to blow at the same speed and from the same direction for an extended length of time.

The fully developed sea is considered using a JONSWAP wave spectrum with peak factor, γ of 3.3 is used in all the sea states, shown in Figure 14. These environmental conditions are used in the global loading [104–112]. The main parameters including zero-up-crossing period T_z, significant heights H_s, and peak period T_p, are presented in Table 7. The JONSWAP Spectrum has been widely used to simulate global wave conditions. The JONSWAP spectrum is modified originally from the Pierson–Moskowitz spectrum [113–116], as given in Equations (49)–(50), to take care of regions that have geographical boundaries, so as to limit the fetch as regards the wave generation. Other terms on the formulation are given in Equations (49)–(53). Irregular waves were used in the analysis.

$$S_\eta(\omega) = exp\left[-\frac{5}{4}\left(\frac{\omega_p^4}{\omega^4}\right)\right]\gamma^a \tag{49}$$

$$S_\eta(\omega) = \frac{\alpha g^2 \gamma^a}{\omega^5} exp\left(-\frac{5}{4}\frac{\omega_p^4}{\omega^4}\right) \tag{50}$$

$$a = \exp\left[-\frac{1}{2\sigma^2}\left(\frac{\omega_p}{\omega} - 1\right)^2\right] \tag{51}$$

$$\sigma = \sigma 1 \; for \;\; \omega_p \leq \omega \tag{52}$$

$$\sigma = \sigma 2 \; for \;\; \omega_p > \omega \tag{53}$$

where S_η is the spectral density, f is frequency in Hertz, ω is angular frequency, ω_p is the peak angular frequency, g is gravitational constant, η is the incident wave amplitude, γ is the peak enhancement factor, while the other parameters σ, σ_1, σ_2 are spectral width parameters. These are also dependent on the significant wave height, H_s and the zero-crossing period, T_z. According to [86], the constants for sigma, σ_1 = 0.07, and σ_2 = 0.09.

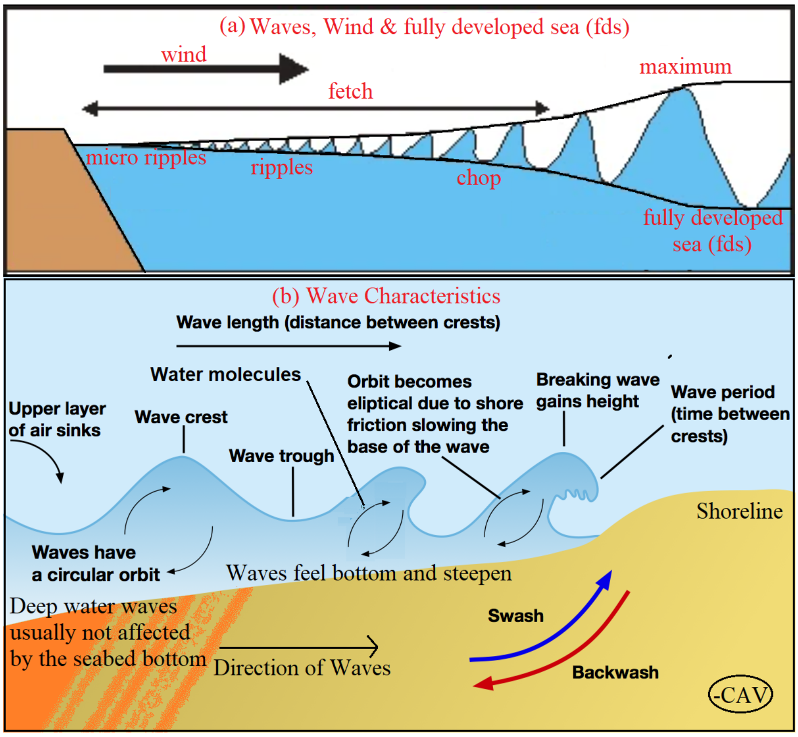

Figure 13. Illustration of: (**a**) wind, waves and Fully Developed Sea (fds) profiles, and (**b**) wave characteristics.

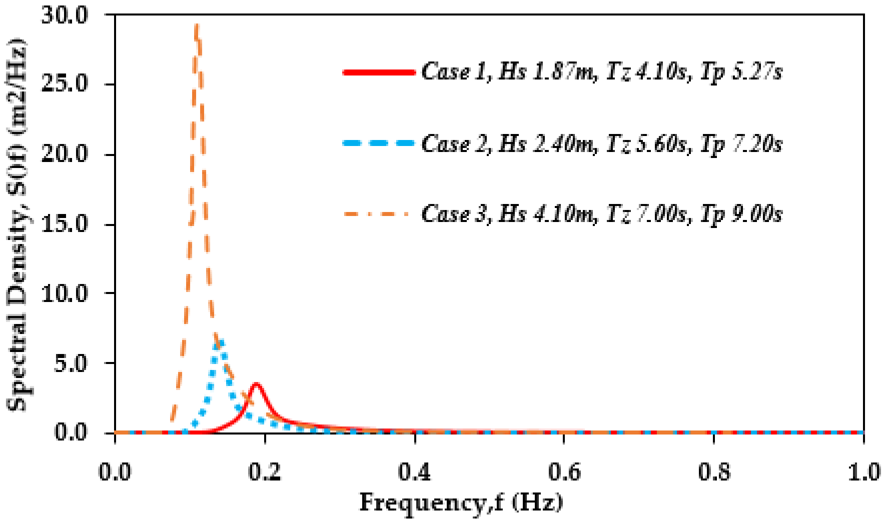

Figure 14. JONSWAP Spectrum for the 3 Sea States or Environmental Cases.

Table 7. Wave Parameters for the 3 load Cases.

Case No.	H_S (m)	T_Z (s)	T_P (s)
1	1.87	4.10	5.27
2	2.40	5.60	7.20
3	4.10	7.00	9.00

2.5.2. Wind and Current

The wave spectrum used for the investigation is JONSWAP spectrum. For the load estimation, the uniform current profile was considered, and wind loads were added to the CALM buoy model. At sea level and at 15 °C, air has a density of approximately 1.225 kg/m^3 (0.001225 g/cm^3). The current speed employed was 0.5 m/s, while the wind speed was 22 m/s, respectively. The current profile for the surface current and seabed current were represented in the XY axes, as detailed in Table 8 and Figure 15a–c. Some parametric studies were carried out, as presented in Section 4. The surface current speed was applied in Orcaflex 11.0 f with power law's current profile [73,74], which must be greater than or equal to current speed at the seabed. The wind and current load coefficients were recorded from a response study on the CALM buoy using ANSYS AQWA, as shown in Figure 15d,e, and the lowest frequency; the fundamental frequency applied in the study was 0.06048 Hz.

Table 8. Wind and Current Parameters.

Parameter	Value
Wind Speed (ms^{-1})	22.00
Wind Type	Constant
Density of Air (gcm^{-3})	0.001225
Kinematic Viscosity of Air (m^{2}s^{-1})	0.000015
Power Law Exponent	7.00
Current Method	Power Law
Current Direction (°)	180
Surface Current (ms^{-1})	0.50
Seabed Current (ms^{-1})	0.45

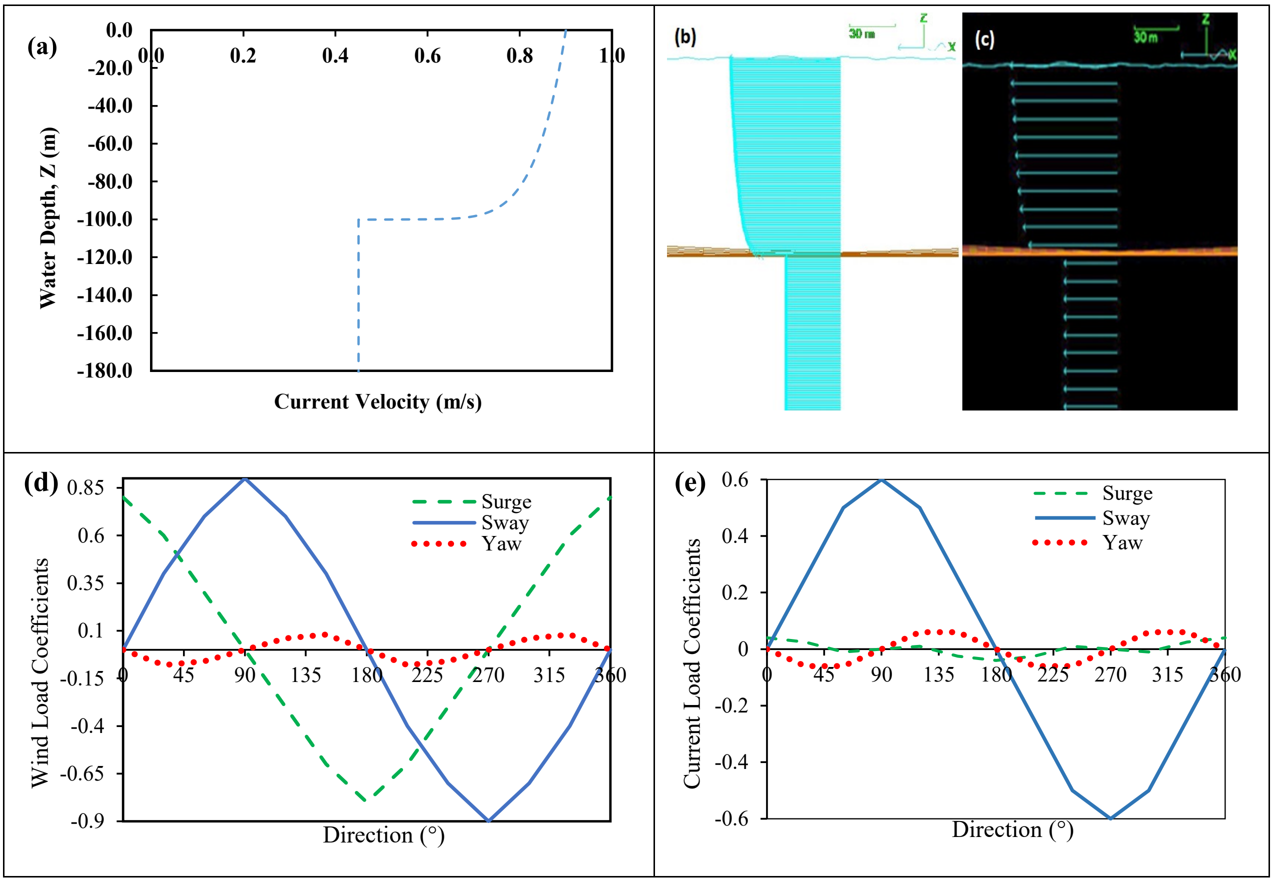

Figure 15. Profiles showing details of (**a**) the vertical profile for Surface Current and Seabed Current at seabed origin, and (**b**) the Orcaflex 3D current profile for both currents, (**c**) the Orcaflex 2D current profile for both currents, (**d**) Load Coefficient for Wind on the CALM buoy, and (**e**) Load Coefficient for Current on the CALM buoy.

2.5.3. Global Loading

In global loading, the three environmental conditions in Table 7 and the three cases given in Table 9 were considered. The loading time history for the wave cases is presented in Figure 16. The plot in Figure 16 accounts for motion, but there is a response from the first order motion in a longer time-frame. It comparatively presents the three load cases beyond the fully developed sea condition, by showing the time-series towards the end of the sea development under harsh conditions of 30 h (108,000 s). It also shows the wave elevation time-series at a chosen location on the sea for the 3 sea states.

Table 9. Definition of Case Study for the 3 Environmental Cases.

Case Study	Flow Angles (°)	Hydrodynamic Loads (HL)
1	0,30,60,90,120	Hose with HL, Hose without HL
2	0,30,60,90,120	Hose with HL, Hose without HL
3	0,30,60,90,120	Hose with HL, Hose without HL

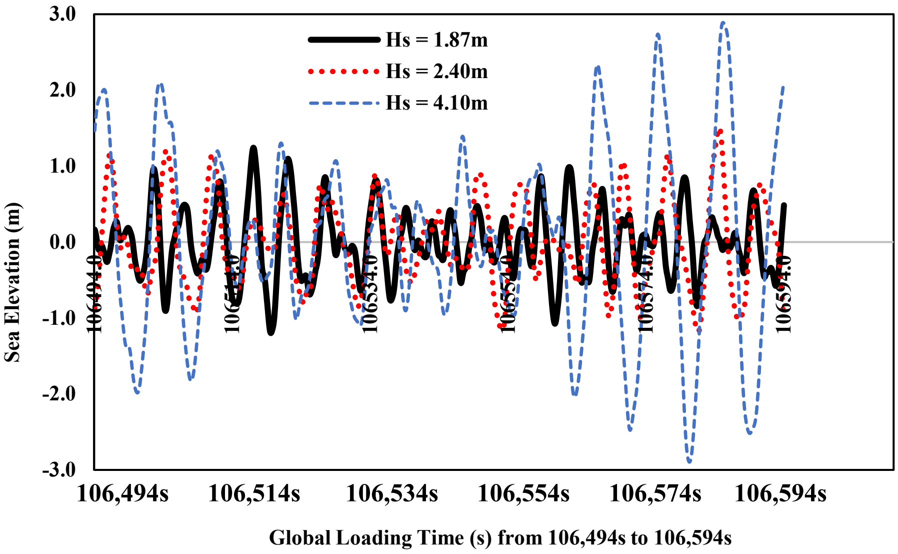

Figure 16. Wave Loading Time History for the 3 Environmental Cases.

2.5.4. Hydrodynamic Damping

The hydrodynamic damping on this study was carried out with an irregular wave. The modified Morison Equation [64] was considered in the calculation of the damping of the buoy with respect to the earth, and considered in the Damping Matrix from ANSYS AQWA [75,76]. Parameters of the hydrodynamic coefficients are given in Table 10.

Submarine hoses are slender bodies, so in this study, the damping is evaluated by applying the modified Morison Equation, given in Equation (54), where D is the diameter of the body, V_r is the relative velocity of fluid particles, V is the volume of the body, A is the area of the body, C_a is the added mass coefficient, C_d is the drag coefficient and C_m is the inertial force coefficient.

$$F = \rho V\dot{u} \ + \rho C_a DA + \rho C_d A(V_r)|V_r| \tag{54}$$

2.5.5. Added Mass and Drag Force

The obtain the added mass and the drag force of the buoy, diffraction and radiation analyses are conducted in ANSYS AQWA using the frequency domain. The hydrodynamic properties are as detailed in Section 2.2. Considering the CALM buoy, the matrix of the RAO was obtained in a LIS file in a beta mode of ANSYS AQWA. Then, it was imported into the Orcaflex 11.0 f. Within this section, the hydrodynamic properties, including the drag forces from both the drag and inertia, will be calculated by lines. This is numerically evaluated initially by using a series of equations, as presented in Section 2.1.

Table 10. Parameters for Hydrodynamic Coefficients.

Parameters	Value
Drag Coefficient, C_d	0.7
Inertia Coefficient, C_m	2.0
Added Mass Coefficient, $C_a = C_m - 1$	1.0
Normal Added Mass Force Coefficient	0.7
Axial Added Mass Force Coefficient	1.1

2.5.6. Mesh Convergence

The mesh convergence is the validation method considered for the hydrodynamic model. It was carried out numerically by carrying out an extensive meshing convergence analysis in the diffraction study in ANSYS AQWA R2. A tolerance of 0.01 m and the maximum element size of 0.25 m were considered. In order to ensure that the effective mesh density was obtained, the range of the elements was from 1.25 m to 0.25 m. The convergence study was carried out using the panel model of the CALM buoy under ocean environment to study the tension, surge displacement and bending in the surge motion. The RAO values were obtained from the hydrostatic parameters, such as potential damping and added mass. For the convergence study, a single wave angle 0° was considered. Table 11 is the results obtained from the effect of the maximum surge RAO that acts along the 0° incidences. The study showed that there were very small deviations in the RAOs obtained from the maximum at 0.25 m element size. Precisely, it is a lot less minimal (<<4%), which infers that the tolerated deviation considered in this analysis will save computational resources and be sufficient, acceptable, and able to validate this research.

Table 11. Mesh Grid independence for Surge Study using diffraction analysis.

Size of Element (m)	Number of Nodes	Number of Elements	Max. Surge RAO (m/m)	Max. RAO Deviation on 0.25 m
1.25	1144	1113	1.18470	0.0827%
1.0	1632	1593	1.18540	0.0556%
0.5	5564	5489	1.18627	0.0187%
0.35	10728	10623	1.18650	0.0099%
0.25	20303	20156	1.18664	0.0000%

2.6. Model Validation

The model validation on this study involves three aspects. These are the numerical model, the real-time model and a physical/experimental hose model. In this present study, the model validation involves the comparison of the hose model and the Orcaflex model in static modes, using the catenary equations given in Equation (55)–(56). The parameters used are the tension forces along the hose ends located at the hose's top position. These are: T_h, the horizontal tension component and T_v, the vertical tension components. Prelimianary assessment of the hose configurations were considered in the hose configurations using some analytical models of the catenary equations [101,102].

The governing equation used in the calculation of the statics for the mooring lines is the Catenary Equation. It is also applied in other applications, like steel catenary risers (SCR) and cable structures [8,98–102]. In the case of mooring lines, they suspend from the PC semi to the anchor on the seabed, and thus take a catenary shape that is approximate, and defined by the following Equation (57), where w denotes weight per unit length, z is height above seabed, w_s is submerged weight, θ is angle to the horizontal axis and s is arc length and H denotes the tension along the horizontal component.

$$T_v = w_s \cdot s \tag{55}$$

$$T_h = \frac{z \cdot w_s}{(\tan\theta)^2} \cdot \left(1 + \surd\left(1 + (\tan\theta)^2\right)\right) \tag{56}$$

By rearrangement of terms, we have:

$$y = \frac{H}{w}\left[\cosh\left(w\frac{x}{H}\right) - 1\right] \tag{57}$$

$$T_h = \omega\left[\frac{s^2 - h^2}{2 \cdot h}\right] \tag{58}$$

$$T = T_h + h \cdot \omega \tag{59}$$

The catenary equations for CALM systems are presented in Equations (55)–(61), where h (or z) denotes the height above seabed, s denotes the arc length, x denotes the section length of the mooring cable, w_s denotes the submerged weight, T_H denotes the tension along the horizontal component, T_v denotes the tension along the vertical component, T denotes the tension component along the plane, V denotes the body's volume and W denotes the body's weight. The schematic of the catenary mooring system of CALM Buoy is illustrated in Figure 17.

$$x = \frac{T_H}{\omega} \cdot ln\left[\frac{T}{T_H} + \sqrt{[\left(\frac{T}{T_H}\right)]^2 - 1}\,\right] \tag{60}$$

$$X = h + X_O - s + x \tag{61}$$

Table 12 shows the findings of both the finite element analysis and the analytical computations. For vertical tensions, the analytical and finite element estimates are 81.6 kN and 78.5 kN, respectively. The horizontal tensions have higher profiles for the analytical and finite element results, as 109.3 kN and 115.4 kN, respectively. As demonstrated in Table 12, there is good agreement between the two techniques, with deviations of 5.3% and 3.9% for the horizontal and vertical forces, respectively.

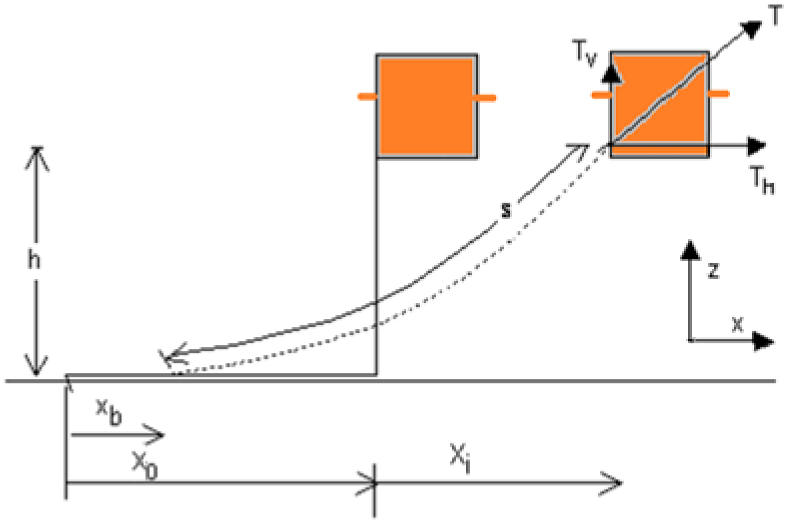

Figure 17. Schematic of Catenary Mooring system of CALM Buoy.

Thirdly, the dynamic effects offered by Orcaflex were examined on the catenary S-lay pipeline through recently completed testing runs (sea trials), based on the confirmed static models [40], and a CALM buoy hose model test conducted in Lancaster University wave tank ([8,26,36]). As a result, Orcaflex dynamic models have the capacity for both static analysis and dynamic analysis on the hose in catenary arrangement ([6,8]). The experimental model in the latter test was designed and tested using the buoy model description in Section 2.2.1. The buoy model was used in the physical testing in the wave tank. The model test results were compared with the numerically validated model in the literature ([26]).

Table 12. Validation by comparing the hose values for maximum tension.

Model	T_h, Horizontal Tension (KN)	T_v,Vertical Tension (KN)
Theoretical Model (TM)	109.30	81.60
Finite Element Model (FEM)	115.40	78.50
Model Average = TM/FEM	0.947	1.039

2.7. Coupling Model

A coupled dynamic modelling of ANSYS AQWA and Orcaflex was used in the numerical modelling. Figure 18 shows a schematic diagram of this numerical technique proposed in this research. The hydrodynamic analysis of the floating buoy was carried out using ANSYS AQWA R2 2020 as the methodology for the analysis. Orcaflex 11.0 f is then used to load the amplitude values for the RAO motions [77–79]. The study approach was based on the hose response. Therefore, the buoy′s motion was also investigated, similar to other floating structures. Two phases of the numerical procedure were completed. The hydrodynamic or diffraction analysis was the first stage, and the finite element analysis was the second, as shown in Figure 18. The model advocates for the RAOs to be generated first, and then the RAOs to be inputted using fluid hydrodynamic pressure. These RAOs can be exported using ANSYS AQWA beta mode and then loaded into a finite element analysis as a load mapping processing. The study involves a "coupled" model into Orcaflex, then it uses the hydrodynamic and excitation forces (without diffraction). Orcaflex cannot use the diffraction model, because the finite element formulation of Orcaflex uses line theory, as discussed in Section 2.3. However, the mesh convergence was necessary to investigate the reliability of the model and obtain the convergence parameters tested based on diffraction. Lastly, the motion RAOs are important in such a model to ascertain the effect of the frequency induced on the buoy, as obtained from the diffraction study, and to ascertain the extent of its response to the buoy. However, this is necessary when considering studies on the motion of FOS like floating CALM buoys and floating semisubmersibles [117–119].

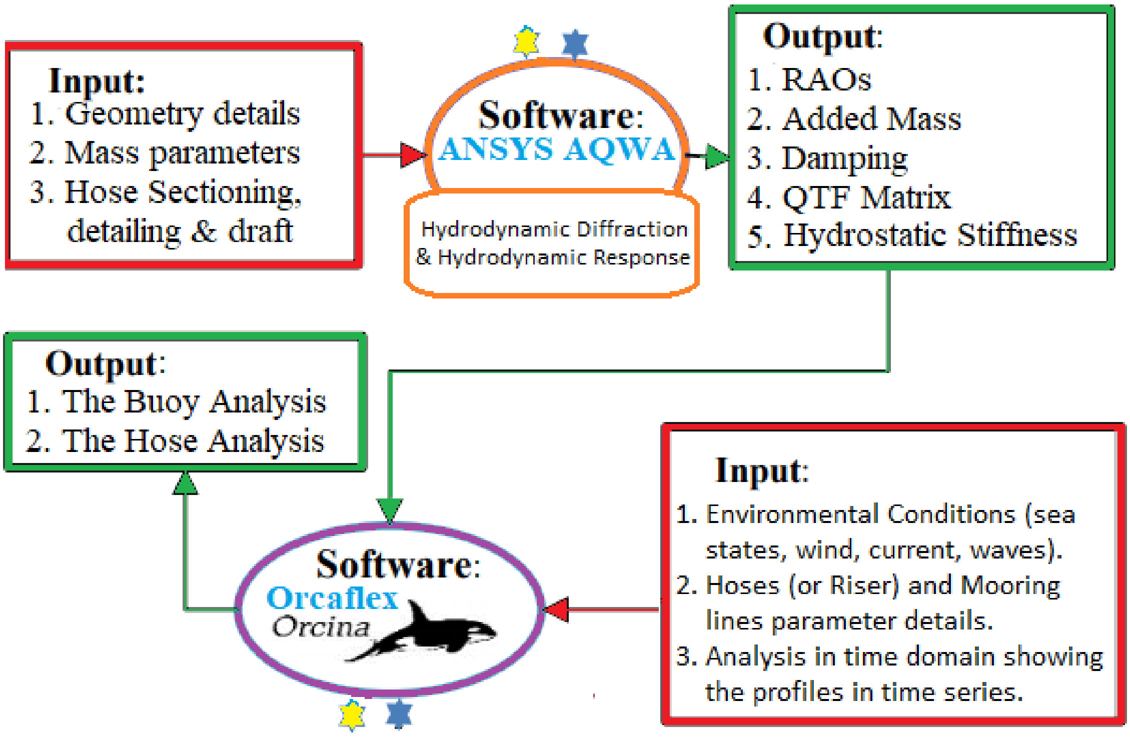

Figure 18. Flow diagram of the methodology for the design analysis.

2.8. Method of Analysis

The methodology for the analysis was conducted by performing the hydrodynamic analysis of the floating free condition for the CALM buoy using ANSYS AQWA. The model of the buoy is free, and devoid of any attached connection, such as mooring line or hoses. This was used to obtain the added mass, radiation damping and RAO. However, the numerical model included mooring lines and hoses in the Orcaflex model, as it was used to investigate the hydrodynamic performance of the submarine hoses. Since the RAOs represent the floater behaviour with buoy hydrostatics presented in Table 13, the motion characteristics from the RAOs generated were loaded into the Orcaflex model. The models are verified using an analytical method. Next, the validated finite element model was carried out with some parametric studies CALM system hoses. For the investigation, the full time for fully developed sea of 10,800 s (3 h) in real time was used for each simulation run in the Orcaflex analysis, with early hose disconnect also considered, as seen in the higher curvature results for extreme cases. The mooring lines for the analysis were in operation and survival modes. Sensitivity studies were also conducted using the wave angles in Section 3. In this study, reference to "wave angle" means "wave direction".

Table 13. Details for Buoy Hydrostatic properties.

Particulars	Value	Unit
Area	438.49	m^2
Volume	344.98	m^3
Buoyancy Force	1,967,500	N
Centre of Gravity	−2.2	m
Moment of Inertia, I_{xx}	4331379.37	$Kg.m^2$
Moment of Inertia, I_{yy}	4486674.11	$Kg.m^2$
Moment of Inertia, I_{zz}	4331379.37	$Kg.m^2$

2.9. Dynamic Amplification Factor (DAF)

Some DAF investigations were also carried out on some of the parameters investigated in Section 3.5. Dynamic amplitude factor (DAF) can be mathematically stated to be the dynamic response amplitude divided by the static response amplitude [70–72], as shown in Equation (62).

$$DAF_{Hose} = \frac{Dynamic\ Response\ Amplitude\ (Including\ hydrodynamic\ loads\ on\ Hose)}{Static\ Response\ Amplitude\ (Excluding\ hydrodynamic\ loads\ on\ Hose)} \quad (62)$$

The advantage of DAF is that the maximum dynamic response amplitude can be determined using the static response amplitude, without any extra requirement for time history analysis. The static response amplitude is the response amplitude operator obtained during static analysis. In real ocean conditions, the amplitude motion of the offshore structure must be accurately predicted and evaluated in the static mode before any offshore operation, with some reliability studies conducted.

3. Results of Numerical Studies

3.1. Sensitivity Studies

A set of sensitivity studies are carried out to investigate the structural behaviour of the hoses, by considering the effect of the hydrodynamic loads. Three different studies are carried out, on the DAF of the submarine hose. They are: the effect of RAOs on the three environmental cases, the effect of RAOs on different flow angles, and the effect of RAOs on different soil stiffnesses. These were used to estimate the curvature, moment and tension values on the hose lines. The hose lines were located as leeside (Hose1) and weatherside (Hose2) on different locations on the nonlinear seabed profile.

3.1.1. Sensitivity to Wave Height and Motion Period

The first step of the sensitivity study is to investigate the effect of wave height and motion period using the environmental cases in Tables 7 and 14. With respect to this, the wave time history in Figure 14 was applied to investigate the effects of wave heights and their respective motion period on the structural performance of the hoses, mainly the curvature, bending moment and effective tension.

Table 14. Cases for Sensitivity of zero-crossing period, Tz.

Cases	**H_S (m)**	**T_Z (secs)**	**T_P (secs)**
T_Z Case 1	1.87	4.10	5.27
T_Z Case 2	1.87	6.50	8.36
T_Z Case 3	1.87	8.30	10.68
T_Z Case 4	1.87	9.66	12.43

3.1.2. Sensitivity to Flow Angles

The effect of flow angle investigated on the submarine hoses was investigated for the following: 0° (stern or following seas), 30° (stern-quartering seas), 60° (stern-quartering seas), 90° (beam seas), and 120° (head-quartering), as shown in Table 9. These correspond to wave progressing directions, with specific details on definition of sea types, as shown in Figure 19.

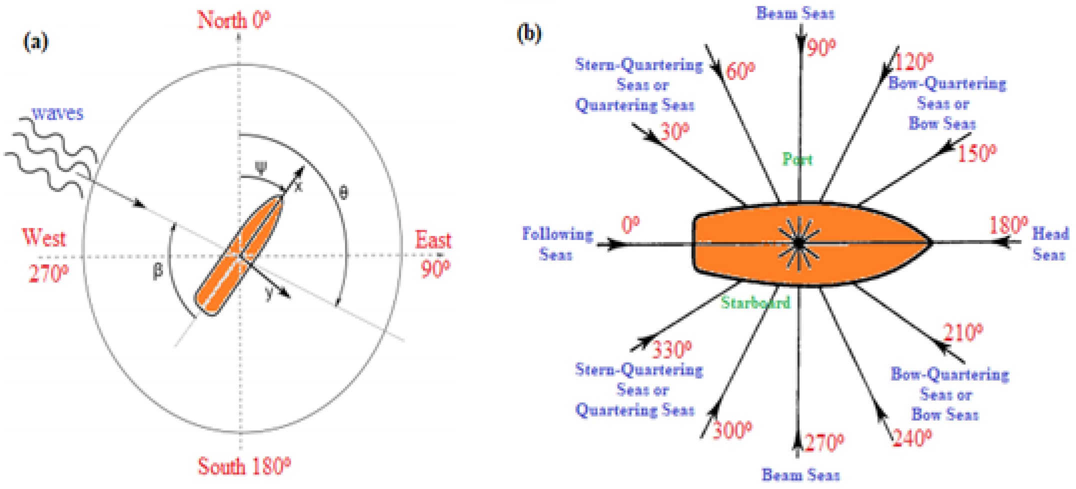

Figure 19. Definition of sea flow angles in approach direction relative to FPSO, showing (**a**) waves on FPSO and (**b**) the wave heading with other different types of seas defined.

3.1.3. Sensitivity to Soil Stiffness

The effect of soil shear stiffness was investigated on the nonlinear model for the following cases: 7.5, 12.5, 25.0, 50.5, 100 kN/m/m^2. Different soil shear stiffnesses were investigated, assuming that the strength of the soil is a function of the soil stiffness [29,50,101].

3.2. Curvature

The curvature profiles along the arc length of the submarine hose for the cases including the hydrodynamic loads and excluding the hydrodynamic loads are presented in Figures 20a–d and 21a–d, respectively. For the sensitivity studies, curvature has similar behaviour. Some deformation were observed on sections of the submarine hose these sections on some arc lengths of the submarine hose. Figure 20a–d shows that maximum value for hose curvature was at 7 m hose arc length. In Case 3 with H_s = 4.10 m, it has the highest curvature for the case with hydrodynamic loads, while Case 1 with H_s = 1.87 m had the least curvature. From Figure 21a–d, it is observed that 0° has the highest curvature. With the nonlinear seabed, the repenetration effect is seen on the curvature behaviour of the submarine hoses. The higher the significant wave height, the higher the curvature effect. In addition, the angle of flow also had an effect on the curvature of the hose. This was expected, as the uniform current flow was considered, and the curvature at 0° was highest, and it differed from the curvature at 90°, as presented in the results in Figure 21.

The inflow and crossflow effects show the influence of vorticity. This can be used to see the effect of vortex-induced vibration of the hoses in further studies. It should be noted that disconnection mode was considered here; as such, the high curvature profiles were from the hose mode during disconnection; thus, it appears to be averagely above 1.0 but it when it is not a disconnection mode, the values are averagely 0.75, depending on the hose section, but not scoped in this paper. (Further research on it is in the authors' thesis publication [26]).

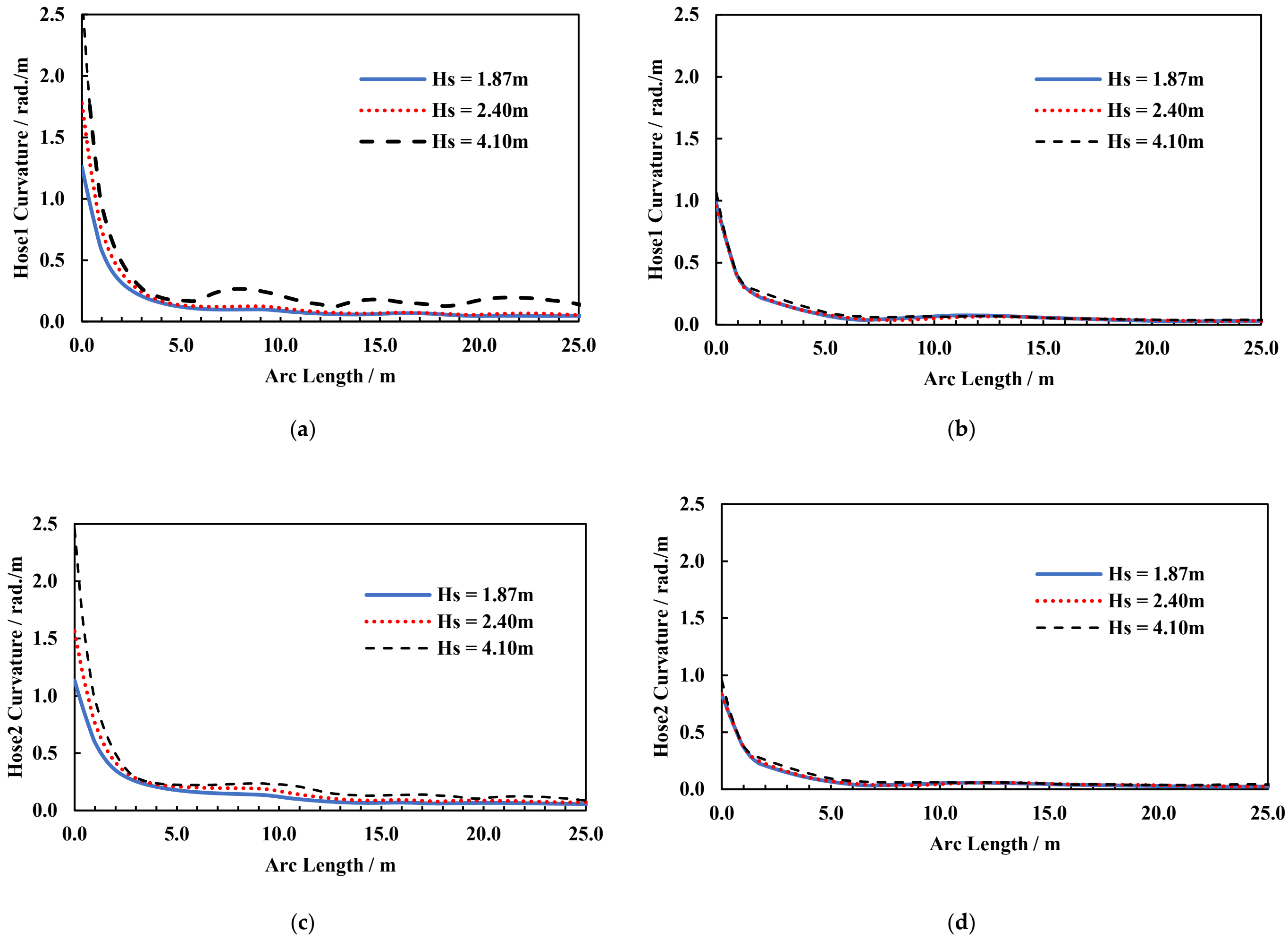

(**a**) (**b**) (**c**) (**d**)

Figure 20. Influence of RAOs for different environmental cases on hose curvature. Figure (**a**,**c**) are when the hoses have RAO loads, while Figure (**b**,**d**) are when the hoses are without RAO loads for the submarine hoses in Lazy-S config. (**a**) Hose1 Curvature including hose hydrodynamic load. (**b**) Hose1 Curvature excluding hose hydrodynamic load.(**c**) Hose2 Curvature including hose hydrodynamic load. (**d**) Hose2 Curvature excluding hose hydrodynamic load.

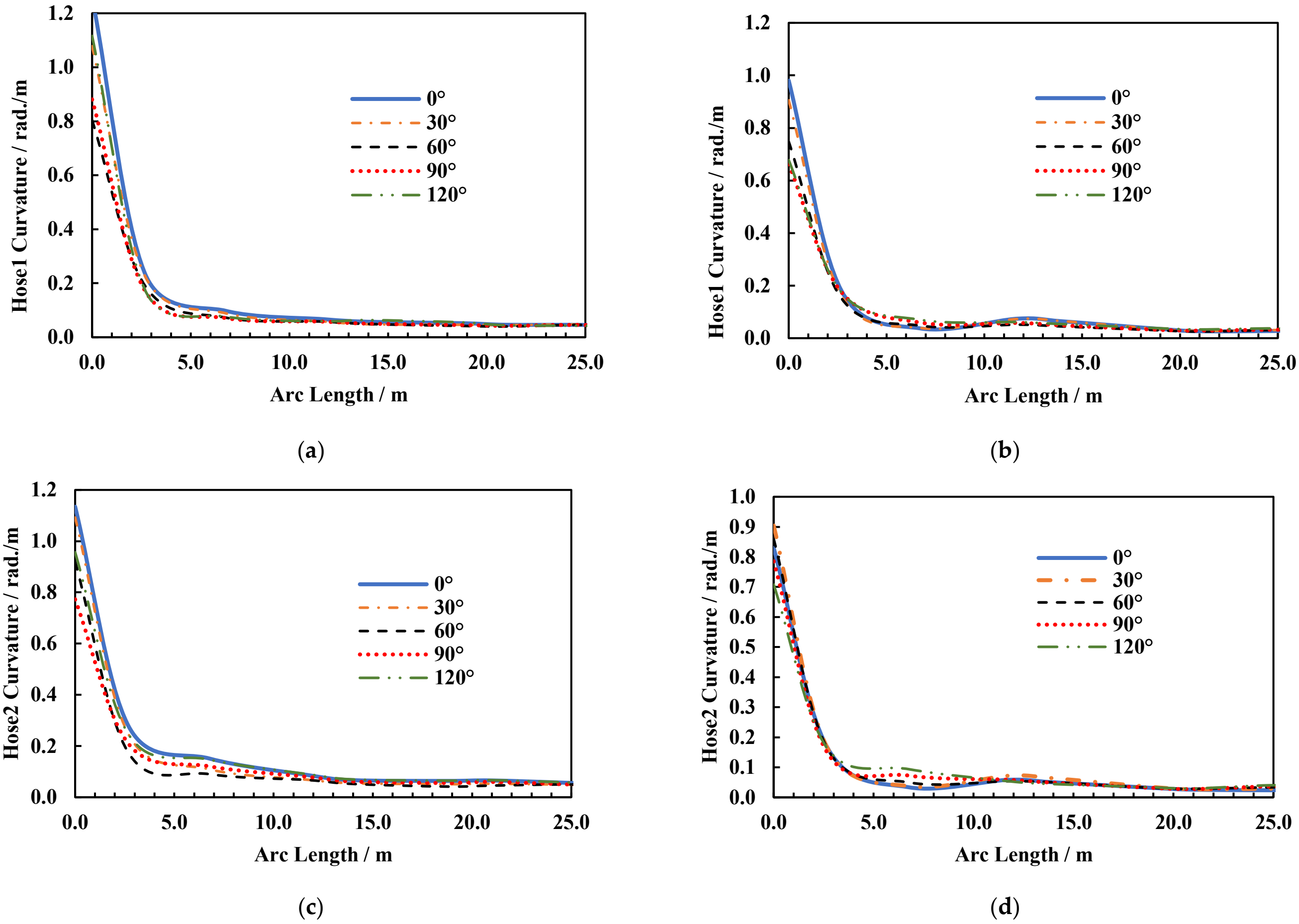

(**a**) (**b**)

(**c**) (**d**)

Figure 21. Influence of RAOs on curvature for different wave directions. Figure (**a**,**c**) are when the hoses have RAO loads, while Figure (**b**,**d**) are when the hoses are without RAO loads for the submarine hoses in Lazy-S config. (**a**) Hose1 Curvature including hose hydrodynamic load. (**b**) Hose1 Curvature excluding hose hydrodynamic load. (**c**) Hose2 Curvature including hose hydrodynamic load. (**d**) Hose2 Curvature excluding hose hydrodynamic load.

3.3. Effective Tension

From Figure 22a–d, the maximum tension is observed at the top reinforced ends, near the restraint underneath the buoy. Moreover, Case 3 with Hs = 4.10 m has the highest effective tension for all the cases investigated, while Case 1 with Hs = 1.87 m had the least effective tension. From Figure 23a–d, a total of 5 flow angles that vary are applied. Models with 120° flow angle particularly presented larger recordings on effective tension over those of 90° flow angle. Models with 90° flow angle also gave larger recordings on effective tension over those of 0° flow angle, except in Figure 23b, which is due to the seabed profile, and nonlinearities in the model. The effective tensions in the simulations with 60° or 120° may increase if the hose hydrodynamic loads are considered. Both ends of the hoses are reinforced and have restraints too. Thus, the hose at each of the two ends has maximum axial and flexural stiffness since the other hose body sections are relatively flexible. However, additional flexible hose sections may have reduced the bending moments, in order to withstand hydrodynamic loadings on the submarine hose-string.

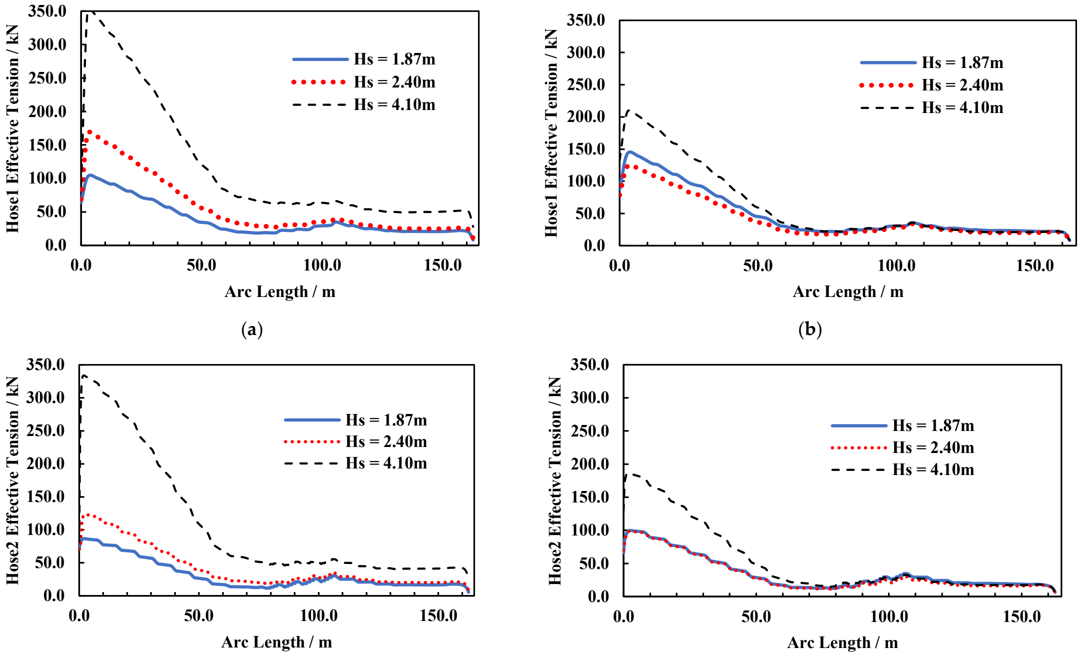

(a) (b) (c) (d)

Figure 22. Influence of RAOs on effective tensions for different environmental cases. Figure (**a**,**c**) are when the hoses have RAO loads, while Figure (**b**,**d**) are when the hoses are without RAO loads for the submarine hoses in Lazy-S. (**a**) Hose1 Effective Tension including hose hydrodynamic load. (**b**) Hose1 Effective Tension excluding hose hydrodynamic load. (**c**) Hose2 Effective Tension including hose hydrodynamic load. (**d**) Hose2 Effective Tension excluding hose hydrodynamic load.

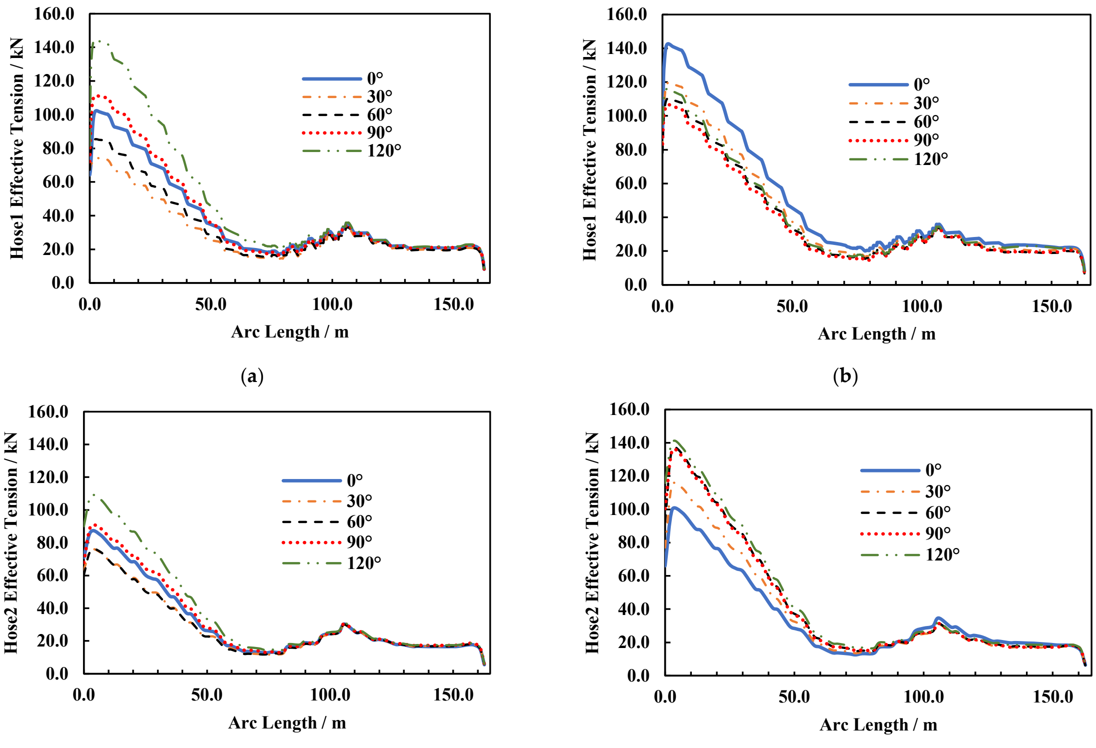

(a) (b) (c) (d)

Figure 23. Influence of RAOs on Effective Tension for different wave directions. Figure (**a**,**c**) are when the hoses have RAO loads, while Figure (**b**,**d**) are when the hoses are without RAO loads for the submarine hoses in Lazy-S config.(**a**) Hose1 Effective Tension including hose hydrodynamic load. (**b**) Hose1 Effective Tension excluding hose hydrodynamic load. (**c**) Hose2 Effective Tension including hose hydrodynamic load. (**d**) Hose2 Effective Tension excluding hose hydrodynamic load.

3.4. Bending Moment

Distributions on the bending moments for the submarine hose-strings are presented in Figures 24a–d and 25a–d. Considering the environmental cases, Figure 24a–d represents the bending moment profiles along the hose arc length for the case studies, including hydrodynamic loads and excluding the hydrodynamic loads. From the results, it is observed that Case 3 with H_s = 4.10 m, has the highest bending moment for all the cases investigated, while Case 1 with H_s = 1.87 m had the least bending moment. This is agreeable with results from Figure 25a–d, because higher periods will intensify the perturbation on the hose system.

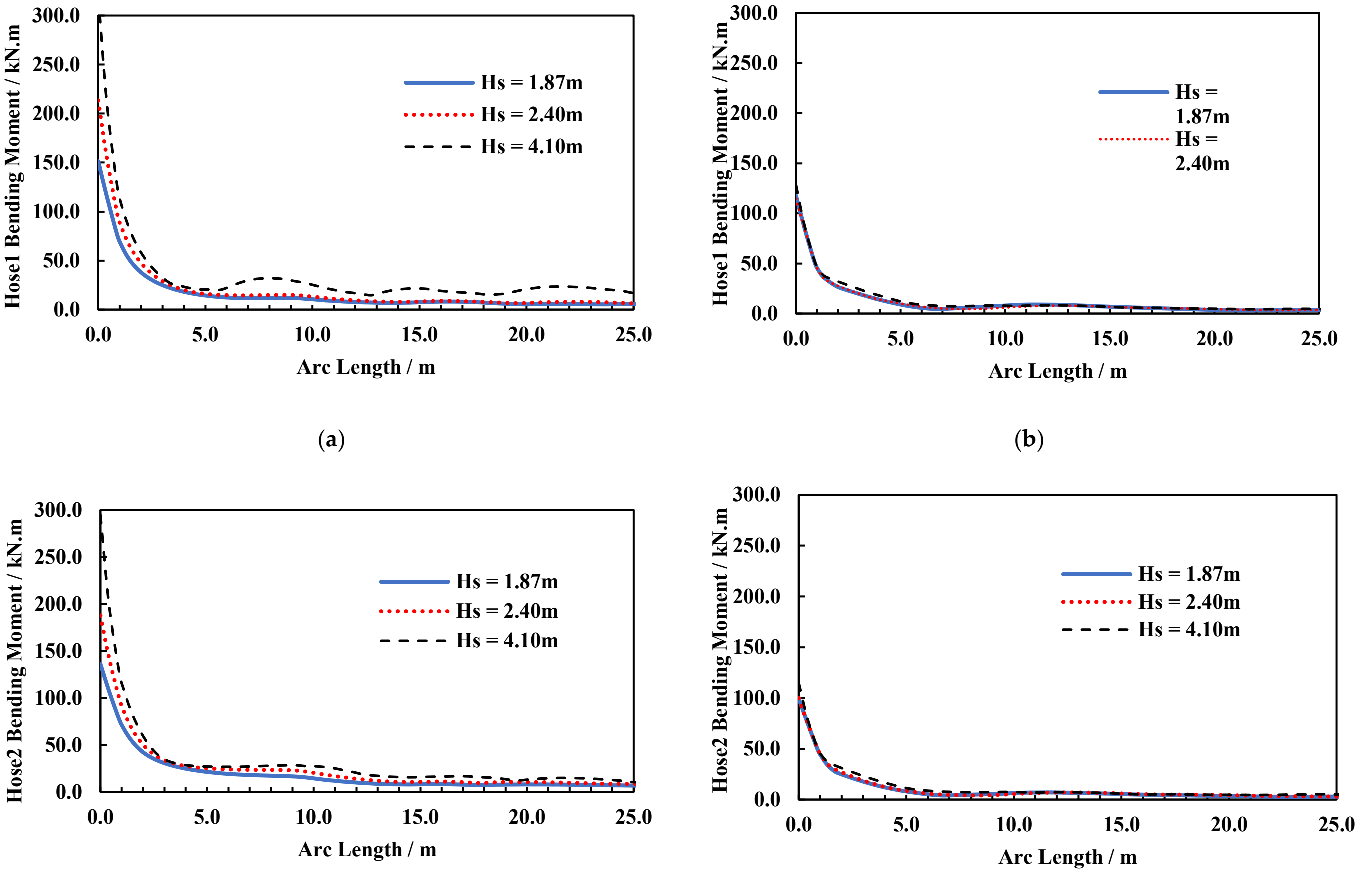

(**a**) (**b**)

(**c**) (**d**)

Figure 24. Influence of RAOs on bending moments for different environmental cases. Figure (**a**,**c**) are when the hoses have RAO loads, while Figure (**b**,**d**) are when the hoses are without RAO loads for the submarine hoses in Lazy-S. (**a**) Hose1 Bending Moment including hose hydrodynamic load. (**b**) Hose1 Bending Moment excluding hose hydrodynamic load. (**c**) Hose2 Bending Moment including hose hydrodynamic load. (**d**) Hose2 Bending Moment excluding hose hydrodynamic load.

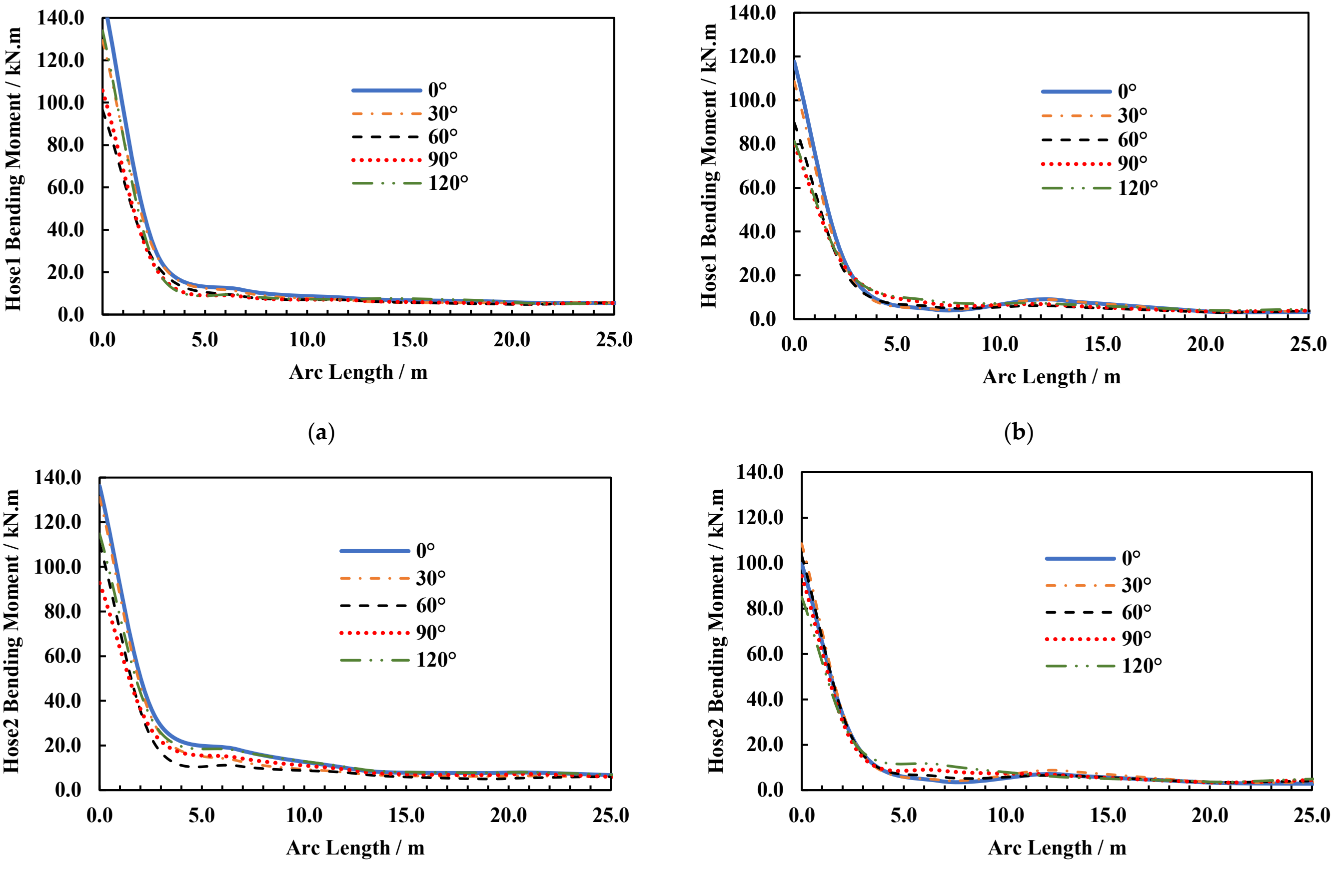

(**a**) (**b**)

(**c**) (**d**)

Figure 25. Influence of RAOs on bending moments for different wave directions. Figure (**a**,**c**) are when the hoses have RAO loads, while Figure (**b**,**d**) are when the hoses are without RAO loads for the submarine hoses in Lazy-S config. (**a**) Hose1 Bending Moment including hose hydrodynamic load. (**b**) Hose1 Bending Moment excluding hose hydrodynamic load. (**c**) Hose2 Bending Moment including hose hydrodynamic load. (**d**) Hose2 Bending Moment excluding hose hydrodynamic load.

3.5. DAF Investigation

Based on the DAF studies carried out, some DAF values were recommended for the submarine hoses in nonlinear seabed, however the values are relative to the position of the submarine hose on the seabed. The DAF_{Hose} along the arc length of the hose are determined for both Hose1 and Hose2 and are presented in Figures 26a–d and 27a–d, respectively. It was also observed that the DAF for Hose2 was higher than the DAF for Hose1, as a result of re-penetration and uplift on the hose on the nonlinear seabed, with respect to its location and position on the nonlinear seabed.

Figure 26a–d gives the profiles for effective tension DAF_{Hose} for Hose1 and Hose2, positioned apart. In an earlier study ([8,9]), a guidance value of 1.0–2.0 was recommended for effective tension DAF_{Hose} and bending moment DAF_{Hose} according to the analyses presented. However, in the present study, the modelling conditions are different, and the hoses were studied during accidental hose disconnection operation, as such curvature is a bit higher. In reality, based on the practical real application scenario, the significant tensions are determined at the touch down zone (TDZ) and connection to PLEM and the Buoy manifold. This can be due to the higher response from wave frequency motion, affected by damping, induced by the wave drift, and perturbed by the nonlinear seabed parameters. As such, the effective tension may be uniformly distributed along the hose body arc length, but varying bending moment. This is also due to the effect of the hydrodynamic coefficients of the buoyancy floats on the hose body. From the DAF curves, the maximum bending moment was obtained at the connections as a result of the high viscous drag on the floating buoy. Therefore, a lower drag coefficient, C_d of 0.7 and the damping coefficient, C_v of 1.0 are used to offset the first order, exciting forces acting as the buoy wave loads.

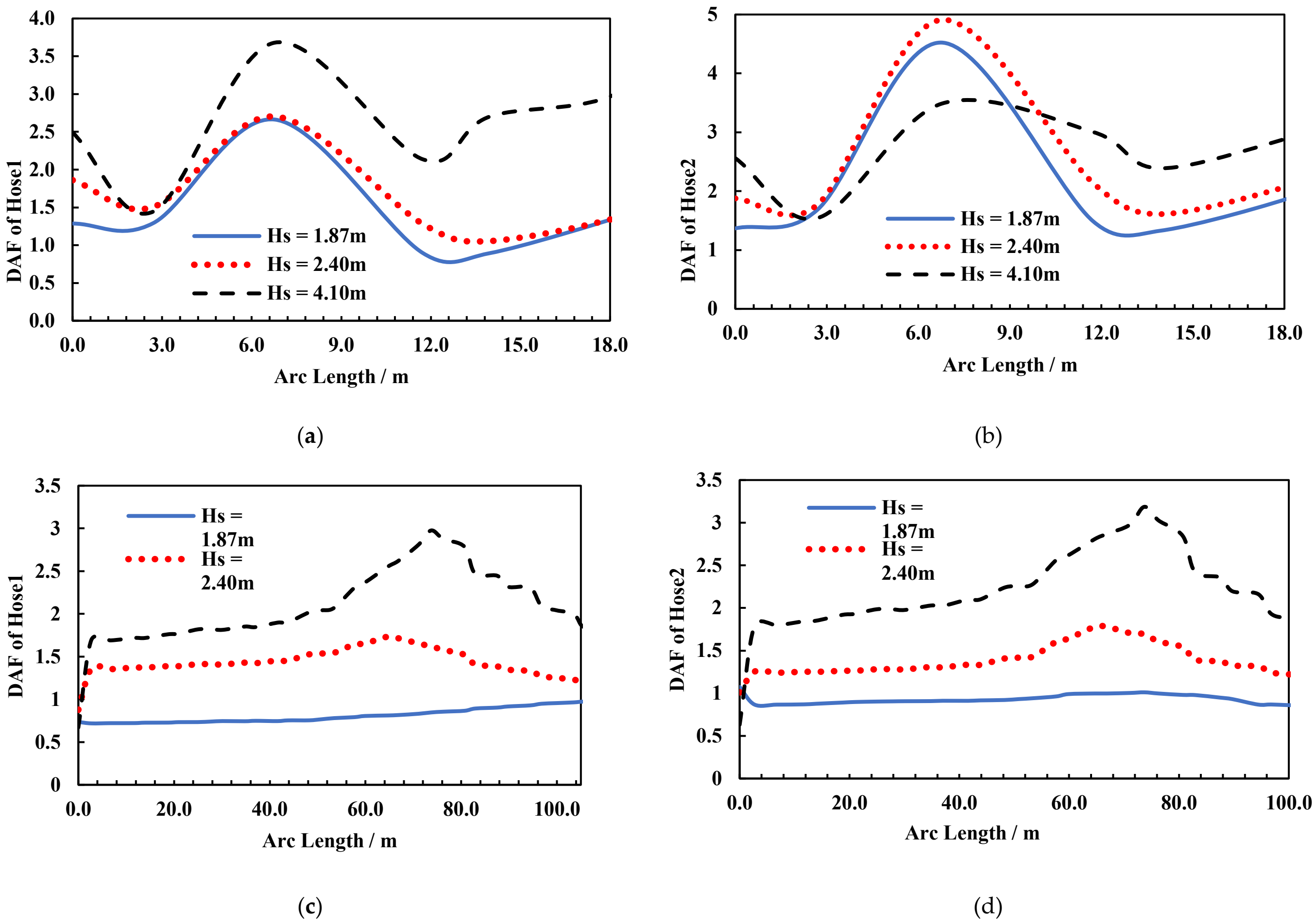

(**a**) (**b**) (**c**) (**d**)

Figure 26. Results on DAF_{Hose} for different environmental cases. Figure (**a**,**c**) are when the hoses have RAO loads, while Figure (**b**,**d**) are when the hoses are without RAO loads for the submarine hoses in Lazy-S config. (**a**) Bending Moment DAF_{Hose} for Hose1. (**b**) Bending Moment DAF_{Hose} for Hose2. (**c**) Effective Tension DAF_{Hose} for Hose1. (**d**) Effective Tension DAF_{Hose} for Hose2.

4. Results of Parametric Studies

4.1. Effect of Surface Current and Seabed Current

The effect of current was studied, considering both the seabed current and surface current in this research. In the design of a CALM buoy system, the surface current velocity is critical as shown in Figure 27. Some surface current values are utilised to explore its influence: 0.45 m/s, 0.65 m/s, 0.75 m/s, 0.9 m/s, and 1.0 m/s. It can be observed that for a very close range between 0.9m/s and 1.0m/s, the surface current has a different profile as the bending moment and effective tension are in phase to each other but not on same value. The bend radius (curvature) drops, the bend moment reduces, and the effective tension increases as the surface current velocity increases, as shown in Figure 27a,b. The following seabed current velocities were examined while considering seabed currents: 0.35 m/s, 0.45 m/s, 0.75 m/s, and 0.9 m/s. Increases in seabed current velocity have a lower effective tension and a lower bend moment for the same surface current velocity, as seen in Figure 27c,d. Reduced bend radius (curvature), higher effective tension, and bend moment result from a rise in seafloor current velocity.

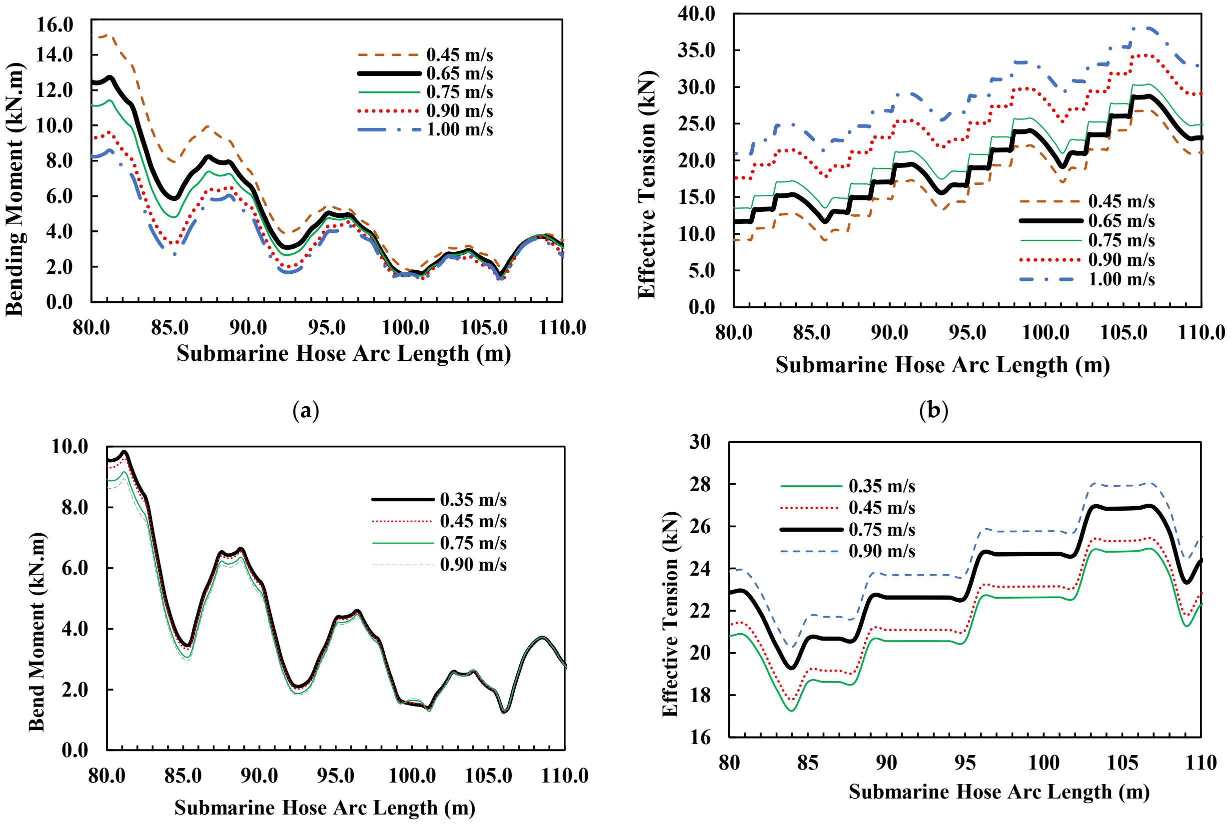

(**a**) (**b**)

(**c**) (**d**)

Figure 27. Result of surface currents (**a**,**b**) and seabed currents (**c**,**d**) on submarine hoses. (**a**) Bending Moment for surface current on arc lengths. (**b**) Effective tension for surface current on arc lengths. (**c**) Bending Moment for seabed current on arc lengths. (**d**) Effective tension for seabed current on arc lengths.

4.2. Effect of Surface Wave Angle (or Wave Direction)

The effect of wave angle investigated on the submarine hoses was investigated for the following: 0°, 30°, 60°, 90° and 120°. The results presented in Figure 28 show that the 120° had the highest tension of 29.21 kN for the investigated submarine hose arc length. However, considering the nonlinear seabed profile, the effective tension may have constant distribution along the hose arc length, but varying bending moment. This is due to the effect of the buoyancy hose on the hoses.

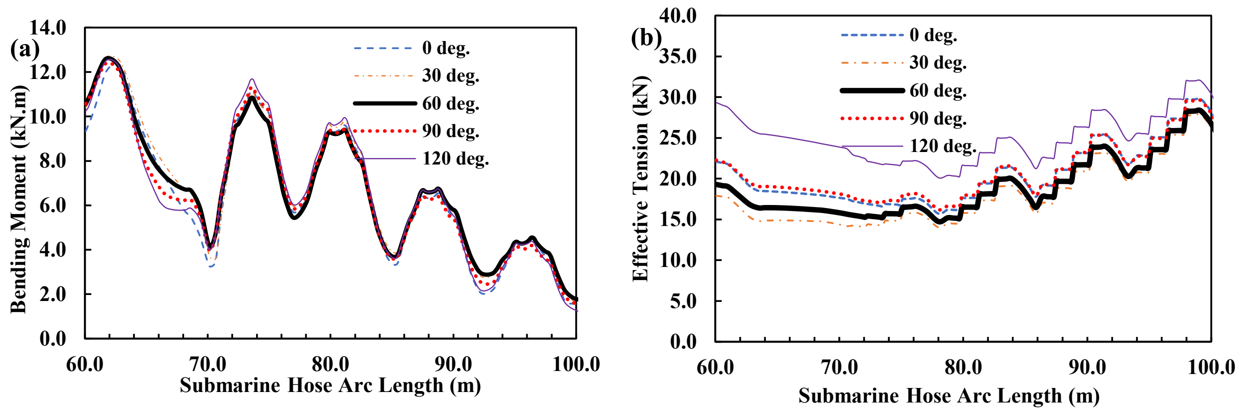

Figure 28. Influence of surface wave direction for the submarine hoses. (**a**) Bending Moment for hose arc lengths 60–100 m. (**b**) Effective Tension for hose arc lengths 60–100 m.

4.3. Effect of Environmental Conditions

The effects of environmental conditions were investigated using the 3 environmental cases in Table 7. From the results in Figure 29a,b, the maximum bending moment and maximum effective tension was observed at Case 3, which is the extreme cases. The operation case did not create much bending and tension that can cause the submarine hose to kink. Thus, the higher the wave significant height and the period, the higher the bending moment and effective tension. The sensitivity study on *Tz* was investigated for 4 environmental *Tz* cases, as presented in Table 14, and Figure 29c,d shows that the *Tz* Case 4 observed the maximum bending moment and maximum effective tension. Thus, the value of the zero-crossing period, *Tz* has a significant effect on the submarine hoses. It can be observed that the surface wave is highly significant in the dynamic responses of the hoseline, which may affect the buoy stability and motion. An increase in the wave height, increases the dynamic responses of the submarine hoses. Thus, the significant height and zero-crossing period, are very sensitive in the buoy's hose performance, as investigated.

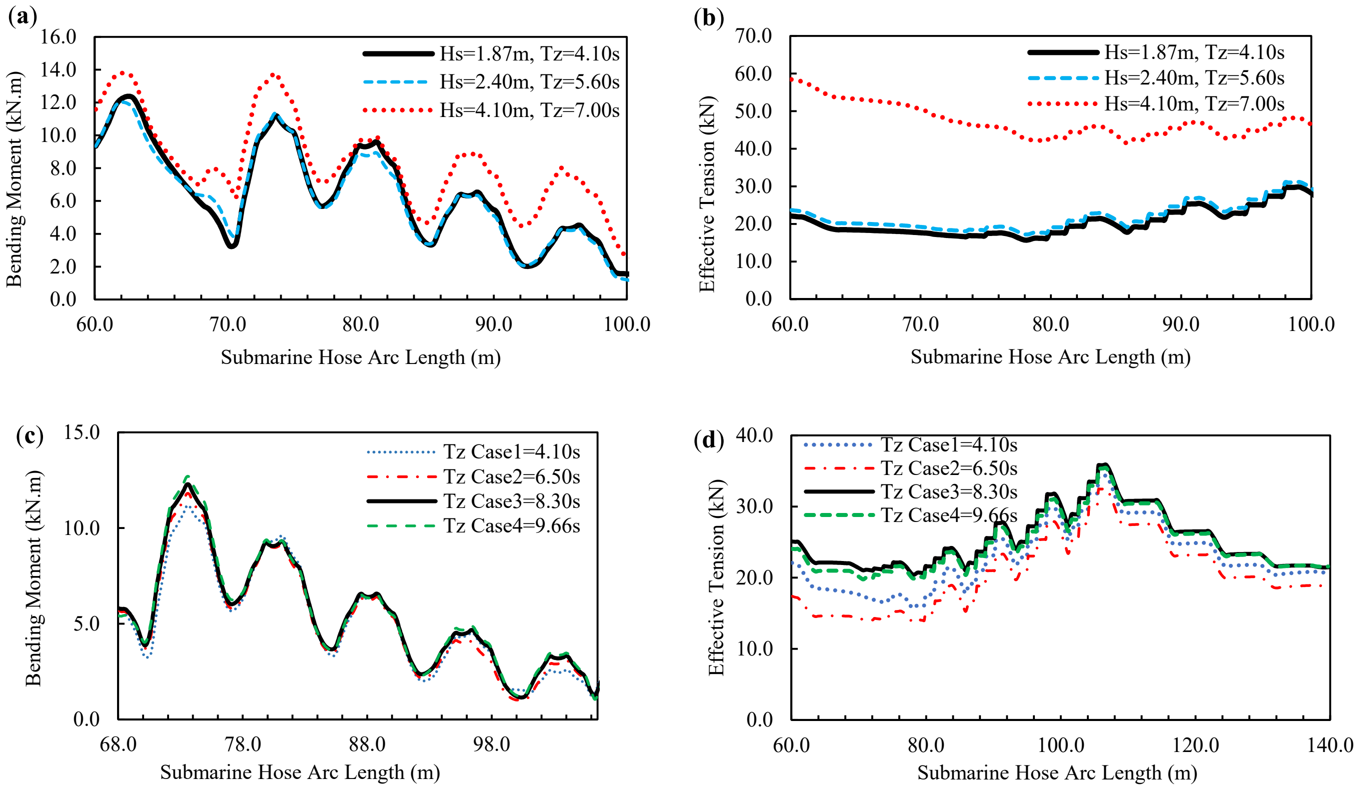

Figure 29. Influence of environmental conditions on submarine hoses. (**a**) Bending Moment for load cases. (**b**) Effective tension for load cases. (**c**) Bending Moment for Tz. (**d**) Effective tension for Tz.

4.4. Effect of Float Outer Diameter

Five different cases with different float outer diameters—0.335 m, 0.350 m, 0.370 m, 0.460 m, and 0.670 m—were investigated. There was no change in the bending moment, and effective tension force, respectively, as investigated on the submarine hose string. They all had the same maximum values, minimum values and static values as presented in Figure 30. With an increase in the outer diameter of the float, using the same hydrodynamic parameters of the floats and the submarine hose, the submarine hose is not affected. Thus, the buoyancy behaviour of the floats is a subject of the hydrodynamic properties of both the float and the submarine hoses.

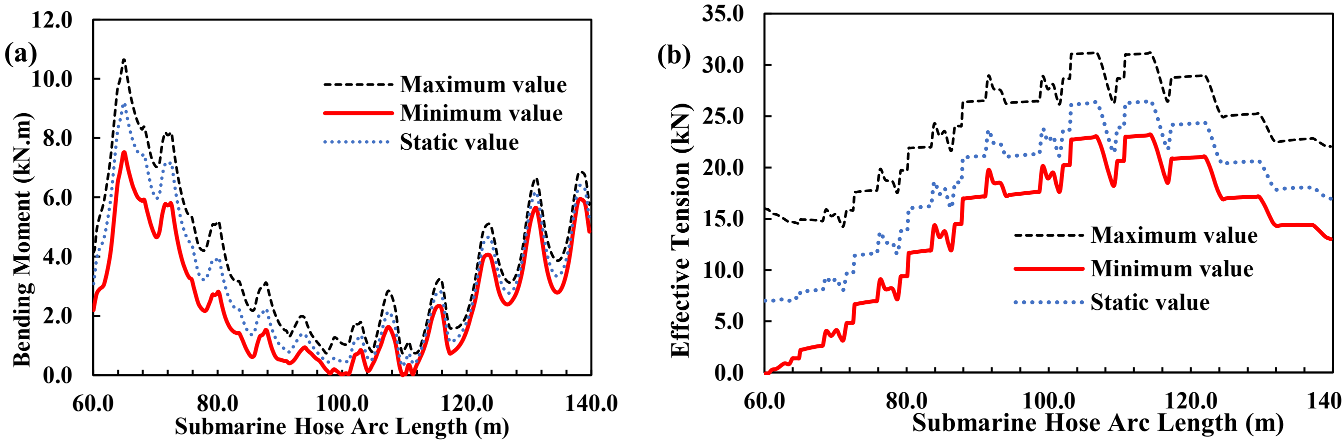

Figure 30. Effect of Float outer diameter on the submarine hoses. (**a**) Bending Moment for hose arc lengths 60–140 m. (**b**) Effective Tension for hose arc lengths 60–140 m.

4.5. Effect of Hose Segment Length

The effect of hose segment length was investigated for three cases with segment length for a section of the hose. This section is the hose body next to the reinforced end (at the end connected to the PLEM). The section has a length of 3.236 m. The cases are presented in Table 15 with the results obtained. The hose segment clearance is the distance from each hose segment to the next hose of a hose-string. In this study, the 3 segments were for Hose1 and considered at the reinforced ends. It was observed that they produced the same tension for the same lengths, but with varying hose curvature. The higher the amount of hose segments, the greater the hose curvature. From Figure 31, the segment with 0.30 m in case 2 has the highest bending moment due to the segment clearance value, with respect to the total segment length. However, this is marginal, with a relatively small difference. The segment clearance in Segment Case 2 is −0.064, which represents a sag in the hose segment. It can be deduced that each hose segment is also a function of its buoyancy and the location on the hose-string. Thus, the location of the hose segments have different bending and tension profiles, as seen in Figure 31.

Table 15. Segment Cases for Hose Segment Lengths.

Segment Cases	Section Length (m)	Segment Length (m)	Number of Segments	Segment Clearance
Segment Case 1	3.236	0.20	16	0.036
Segment Case 2	3.236	0.30	11	−0.064
Segment Case 3	3.236	0.50	6	0.236

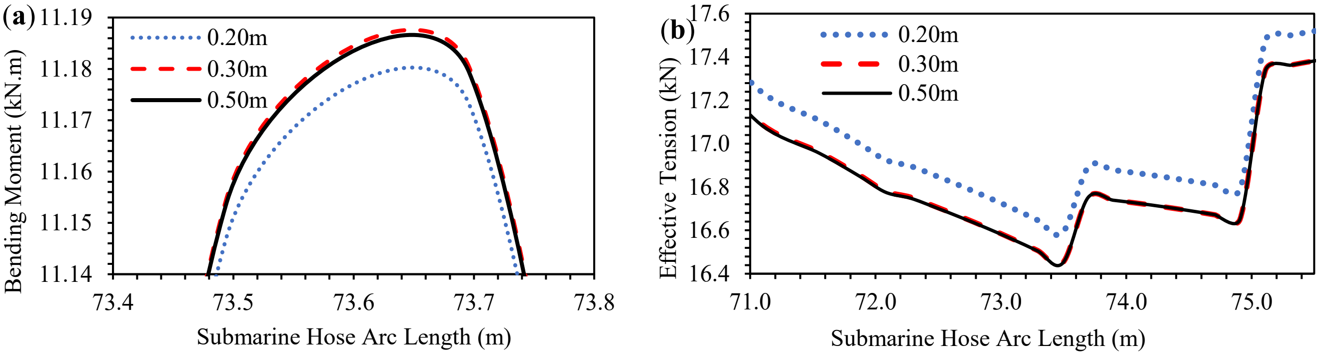

Figure 31. Effect of hose segment lengths of submarine hoses. (**a**) Bending Moment for hose segment lengths. (**b**) Effective tension for hose segment lengths.

4.6. Effect of Float Buoyancy Length Location

The effect of the float buoyancy length location for the 25 floats on the same submarine hose lengths but on varying distances, is presented as in Figure 32. It shows that the float locations for parametric study on float length has a significant effect on the buoyancy of the submarine hoses. Float case 1 had the highest bending moment (BM) while float case 4 had the least. This meant that the weight of the float system in float case 1 was the lowest and this would not be the best in terms of curvature, as it also gave the maximum BM of 6.66 kN.m at hose arc length 131 m.Thus the float type used in that area may need to be replaced with another with better buoyancy to reduce the BM.

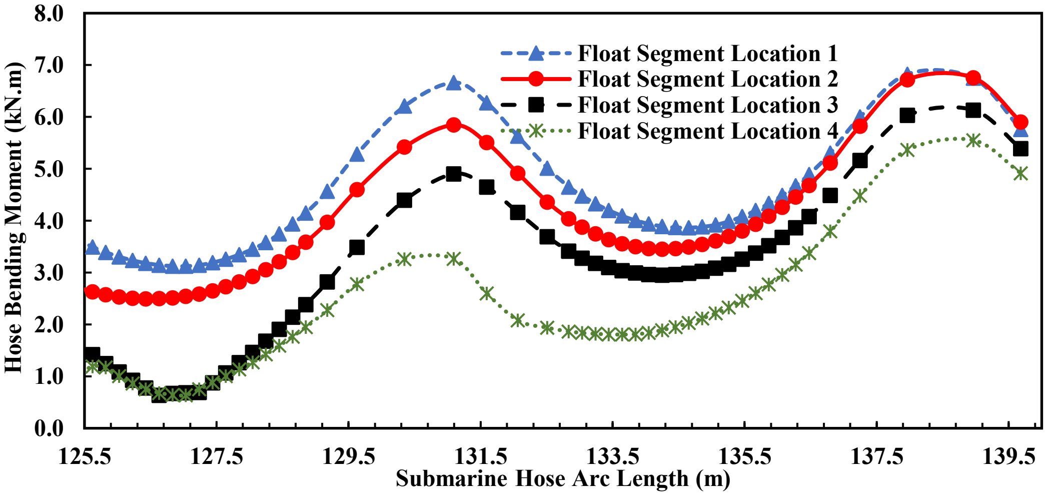

Figure 32. Effect of float buoyancy length location along hose arc length.

4.7. Effect of Seabed Soil Models

The effect of the seabed soil models on the same submarine hose lengths was reviewed. Figure 33a shows that the 3D elastic linear seabed model generates the highest bending moment, followed by the 3D rigid nonlinear seabed model, then the flat elastic linear seabed model, while the flat rigid seabed model recorded the minimum bending moment. Figure 33b shows that the flat rigid nonlinear seabed model generates the maximum effective tension, followed by the flat elastic linear seabed model, then the 3D rigid nonlinear model, while the minimum is the 3D elastic linear seabed model; however, their results are very close. This implies that, when the soil stiffness is carefully selected for the linear seabed model, it will not only give rise to the similarly calculated results of the nonlinear seabed model, but it will save computational resources. In Figure 33c, the linear elastic seabed model has the maximum the seabed normal penetration/D, while the rigid nonlinear seabed model is the minimum. However, in Figure 33d, the rigid nonlinear seabed model has the maximum seabed normal resistance, while the linear elastic seabed model is the minimum, similar to submarine pipeline S-lay in the literature [40,43–45].

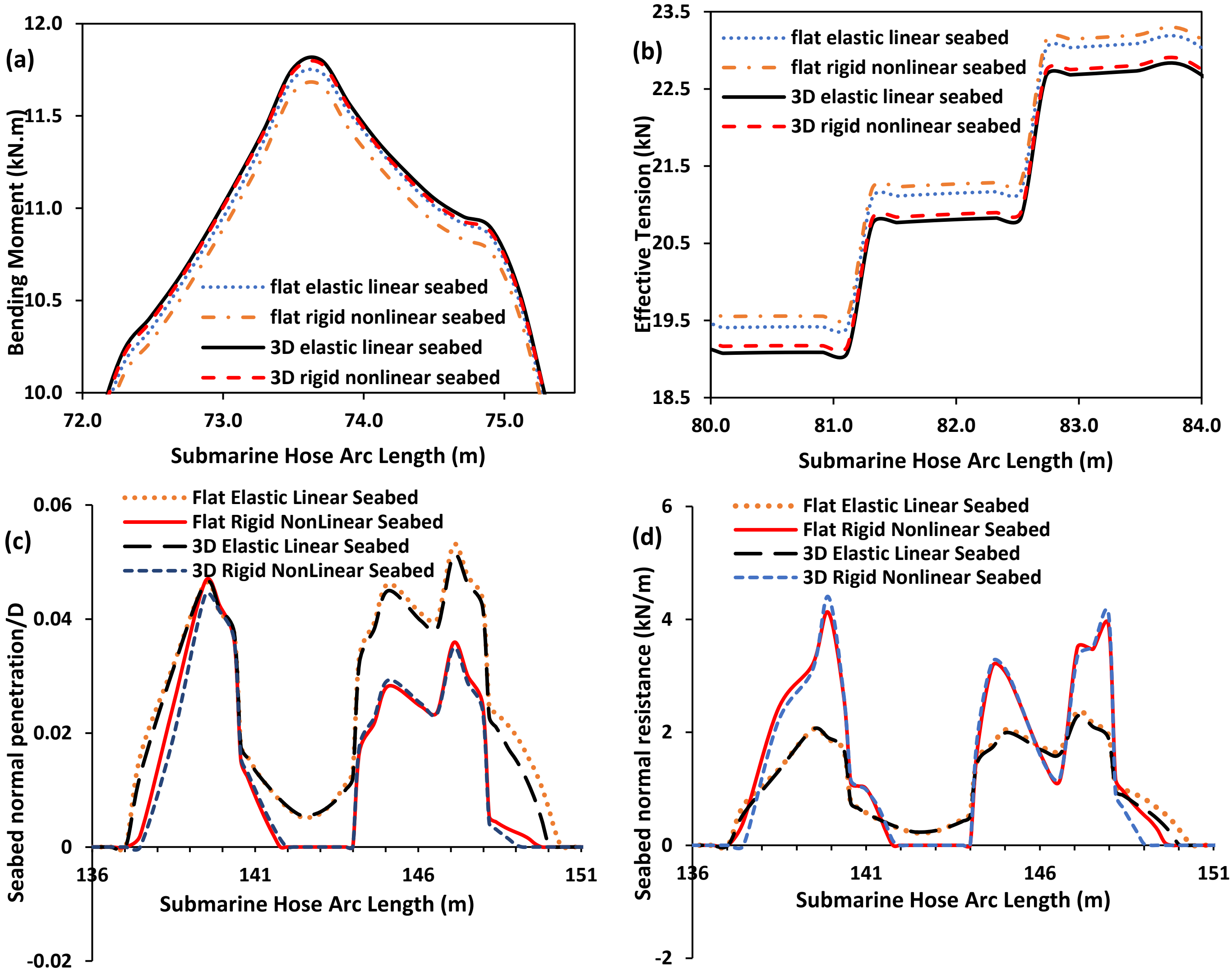

Figure 33. Influence of Seabed Soil Model on the submarine hoses, for (**a**) Bending moment, (**b**) Effective Tension, (**c**) Seabed normal penetration/D, and (**d**) Seabed normal resistance.

4.8. Effect of Water Depth and Hose Static Offset

The effect of water depth was carried out on the offshore hoses in Lazy-S configuration, as given in Figure 34a,b. The effect of the hose configuration was investigated using a water depth of 100m in Lazy-S design during static analysis. As observed in Figure 34a, the maximum results were obtained to be higher than the minimum and mean values, as obtained for the static offset of the offshore hose riser. It shows to be consistent, and the maximum value is used to see the extreme hose behaviour of static offset configuration of Lazy-S. As the water depth increases, it takes the form of a Lazy-S configuration, usually due to the buoyancy design, such as the use of buoyancy floats. In Figure 34b, similar behaviour was observed when compared for linear seabed and nonlinear seabed models. Thus, it also validates the consistency of the proposed model. However, this profile is not generic but unique to this Lazy-S case, as each Lazy-S configuration will change with respect to the environmental loadings of that case, the hose buoyancy, the water depth, the position of the buoyancy floats, and the weight of the marine hose in water. The investigation of the seabed model on the hose-string shows that the linear seabed model has a bit different behaviour than the nonlinear seabed model. As the water depth increase, the configuration in the linear seabed is higher than that of the nonlinear seabed model slightly. This can be due to repenetration, uplift and soil resistance factors. As such, another study is conducted in Section 4.9, to find the maximum soil shear stiffness that will generate the least bending moment, and the least effective tension under (non)linear seabed model. Further studies can include the influence of variation or nonlinearity due to the seabed soil resistance, rate of penetration, and uplift on the seabed.

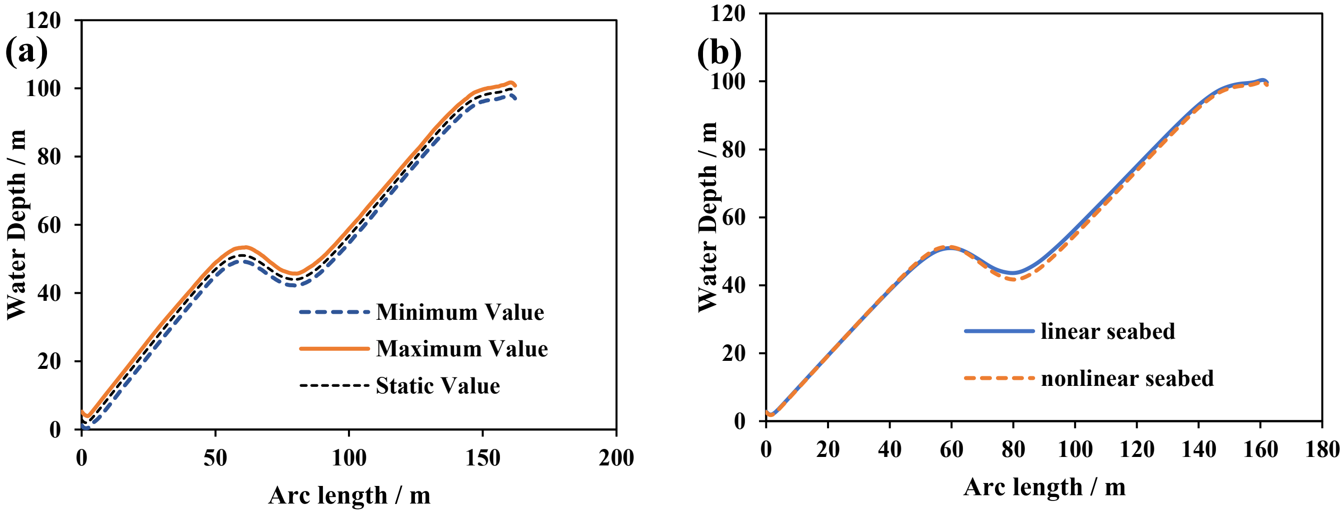

Figure 34. Influence of water depth and hose static offset in Lazy-S configuration on submarine hoses. (**a**) Effect of water depth on static offset configuration of lazy-S hoses for linear seabed. (**b**) Effect of water depth on static offset for linear and non-linear seabeds.

4.9. Effect of Soil Shear Strength Gradient and Soil Stiffness

Figure 35 shows the effective tension profiles along the undersea hose-line for the soil shear strength gradient at 1.0, 1.5, 2.0, and 2.5 kPa/m. As shown in Figure 35a,b, the larger the magnitude of the soil shear strength gradient, the smaller the bending moment and effective strain on the undersea hose-line. As a result, the stiffness of the soil determines its strength. The effective tension, as well as the bend moment, decreases as the soil′s shear stiffness increases. On the nonlinear soil model, the effect of soil shear stiffness was also explored using the soil shear stiffnesses of 7.5, 12.5, 25.0, 50.5, and 100 kN/m/m^2. Figure 35c,d demonstrates that the soil shear stiffness with the highest bending moment and effective tension had the lowest bending moment and effective tension. The influence of variation or nonlinearity due to the rate of penetration, seabed soil resistance, and uplift on the seabed is shown in this work on the 3D nonlinear seabed model, which is similar to pipeline installations in nonlinear seabeds [43–45].

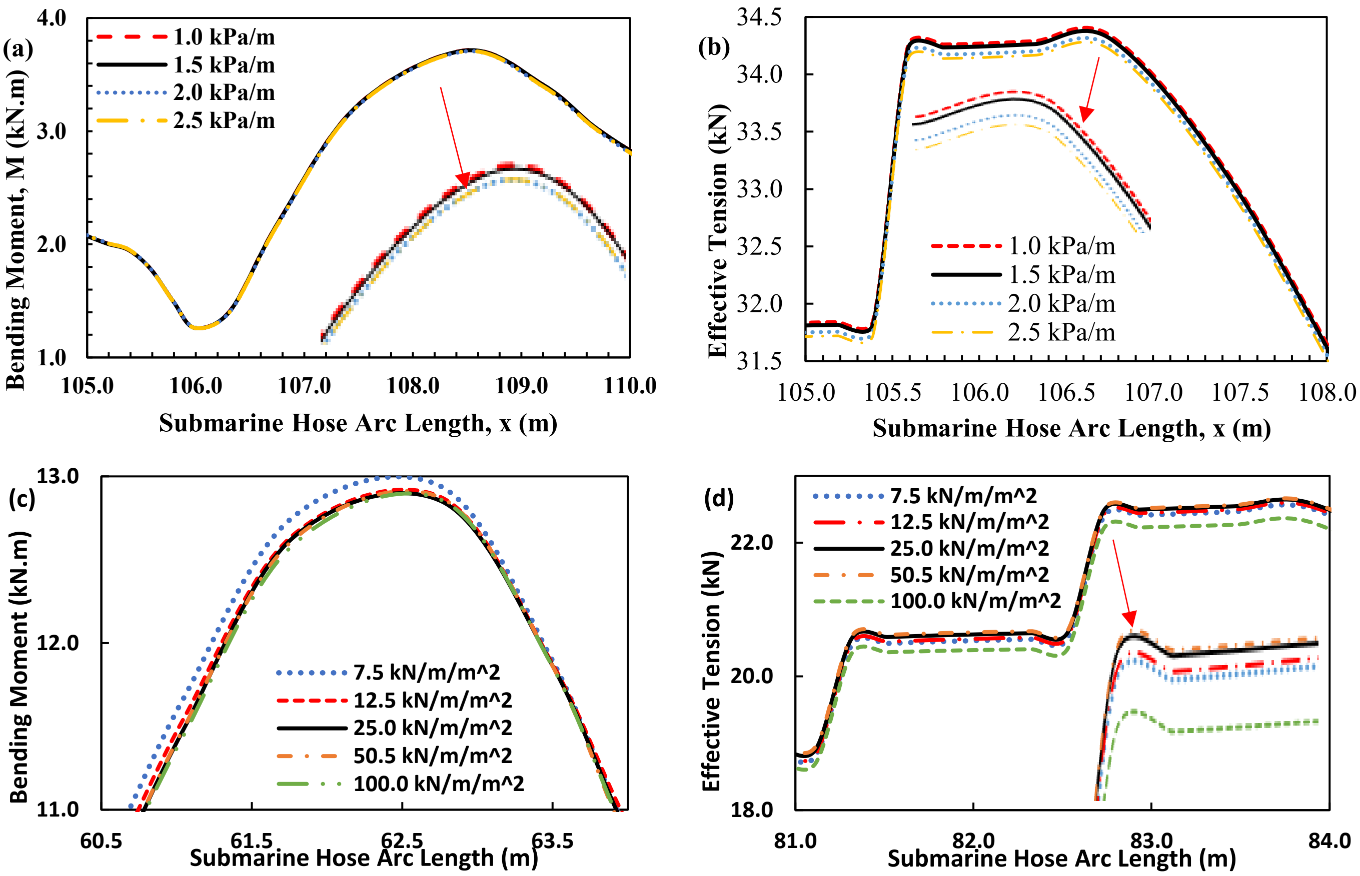

Figure 35. Influence of soil shear strength gradient and soil stiffness on submarine hoses. (**a**) Bending Moment for soil shear strength gradient. (**b**) Effective tension for soil shear strength gradient. (**c**) Bending Moment for soil stiffness. (**d**) Effective tension for soil stiffness.

5. Discussion

This section presents a critical analysis of data, discusses the results further and compared them with other models, as is needed to fully evaluate the scope of the results. Most CALM buoy hose systems exist on linear seabeds which are flat, like in the present model. However, the present study compares both linear and nonlinear seabed models. The nonlinear seabed model as depicted in Figures 34b and 35, and is used to assess the effect of soil resistance and penetration on the hose. The nonlinear seabed models were first carried out on SCRs using Orcaflex line model by Randolph [54–58]. The nonlinear seabed model was considered as hysteretic, using the phenomenon depicted by Figure 12 in Section 2.4. With the nonlinear seabed model, the soil shear strength, gradient, density, buoyancy factor, resistance ratio and penetration parameters are all taken into account.

This study has also shown that vibration control is necessary on marine hoses, as seen in the high prorfiles of the tension, bending moment and curvature in Section 3. Moreover, due to the existence of a nonlinear seabed, the responses of a CALM buoy or those of mooring lines does not become nonlinear. However, the vibration from ocean waves, CALM buoy motion and other perturbation effects can be normalised, stabilised and controlled. In practice, it is necessary to apply considerable control measures on the hoses by using hose-riser control systems, surge protectors, hose couplings and valve connectors are used. Examples of valves coupled to the marine hoses include hose end valve (HEV), butterfly valves, and marine breakaway coupling (MBC). Another method that has been used in tubular marine structures is to increase the material thickness, reported on marine hoses [17–19], composite marine risers [20–26] and pipe-in-pipe (PIP) submarine pipelines [120–124].

On the nonlinear hysteretic seabed model, as proposed in this research, it can be used to quantitatively estimate different parameters for marine hose systems. From this study, it has been used to assess the effect of the soil characteristics, surface wave, surface current, seabed soil models, and motion behaviour on the hose, due to hydrodynamic load. The surface and seabed currents have an influence on the dynamic behaviour of the hoseline. With an increase in the current attack angle, the effective tension increases while the bending moment decreases. For the soil shear strength gradient, as the weight of the hose line is getting onto the soil through the PLEM, the seabed resistance increases.

In this study, the soil stiffness had no major influence on the DAF curves, thus DAF can be seen as independent from the soil stiffness. This is subject to further investigation by considering other parameters in the nonlinear seabed model. In this present study, the effect of soil stiffness and soil gradient displayed some dynamic effects on the hose performance. Unlike SCR and submarine pipeline models, the effect of TDP on submarine hoses is not very high, due to the connections made to the manifold (PLEM). Also, in the case of floating hoses, they are usually surface hoses and do not have issues with undersea actions, and seabed activity.

In a practical sense, lateral stability is one issue that is also challenged by nonlinear seabeds, but it was not considered in this numerical investigation. Thus, there is a need to investigate the influence of lateral stability on the nonlinear seabed model for the submarine hoses. In conclusion, investigations including the DAF sensitivity studies have been carried out successfully for submarine hoses. DAF_{hose} approach can be seen to be very reasonable in the determination of response behaviour of offshore submarine hoses. It also shows the effect of uplift and re-penetration of the nonlinear seabed model on the hoses.

The guidance figures are based on the present study and have been reflected as such. These do not reflect a general case of Lazy-S configurations or nonlinear seabed models. The reason is due to limitations in different models and design specifications, which may differ, such as seabed type, water depth, configuration, hose manufacturer, hose type, etc. However, this can be investigated in further study, due to the universal applicability of DAF on offshore hoses. It is noteworthy to state that DAF is primarily used for fixed offshore structures where the dynamic response is quasi-static. For compliant structures such as submarine hoses and pipelines which are dependent on an existing structure, the dynamic response is highly nonlinear; therefore, the DAF becomes highly dependent on many factors, such as the configuration, the system parameters, the environmental condition, etc. Thus, the DAF_{hose} approach, as applied here, is proposed for both linear and nonlinear seabed models, with Lazy-S configuration on submarine hose systems.

Lastly, the study also presented a relationship between the linear seabed model and the nonlinear seabed model, and found it to be consistent in the model, using some parameters, as presented in Figure 33. Thus, it is an appreciable method to consider that nonlinear seabed profiles can influence submarine hoses as well as submarine pipelines. The angles were steep in some regions; as such, this can also be considered during pipe-laying and installation procedures. Considerations should be made on the marine hose design that will be economical, safe and sustainable. To offset this challenge, the number of buoyancy floats could be increased, and the location of the floats could be redesigned.

6. Conclusions

The dynamic analysis of offshore structural systems like CALM buoys are time consuming and computationally expensive. One reason is that most offshore structures that have slender bodies like mooring lines, marine hoses and marine risers require more mesh grids that are uniform to converge. However, during the simulation process, there are also different sources of nonlinearities in time-domain analysis. Thus, it is necessary to simplify the structural dynamic analyses by applying DAF, which is common practice in structural designs. The advantage of DAF is that the maximum dynamic response amplitude can be determined using the static response amplitude, without any extra requirement for time history analysis. This paper presents numerical studies based on sensitivity and parametric investigations carried out on offshore submarine hoses with respect to hydrodynamic loads, using a nonlinear seabed model.

The model highlights are as follows:

- Numerical assessment on the dynamic behaviour of CALM buoy hoses—a contribution to wave load applications on offshore structures, and pipe laying;
- Application of dynamic amplification called the DAF_{Hose} estimation, which shows the influence of nonlinear seabed model on submarine hoses;
- Hydrodynamic study and sensitivity studies on the hose model show the effect of wave loads on the minimum bearing radius of the submarine hoses,
- Presents wave load cases for the flow on submarine hoses attached to CALM buoy;
- Parametric studies on Lazy-S configuration, which can be useful in offshore industry with the effect of current on the offloading system.

The influence of floating CALM buoys′ wave-induced behavior on the load response of subsea hose systems has been investigated. ANSYS AQWA was used to develop hydrodynamic models for the determination of RAOs of the buoy. The RAOs, together with other important environmental, geometric, and material variables, were used to create the dynamic models on the CALM buoy with hose in Lazy-S configuration. The model was then tested against other models. Then, by changing the wave heights, flow angle, and soil stiffness, a series of sensitivity experiments are carried out. In terms of curvature, effective tension and bending moment; and the effects of the wave direction and hose hydrodynamic loads on the structural reaction of the hose are investigated.

From this study, the influence of soil seabed models on the hose performance has been presented. The higher the soil shear stiffness, the lower the bending moment and effective tension distributions. Moreover, the higher the soil shear strength gradient, the lower the bending moment and effective tension distributions. This implies that the shear forces acting within the soil is less when there is less soil pressure, and subsequently increases the van-de-Waals forces in the soil structure. This, in turn, reflects on the reduces nonlinearities and pertubations that would be induced to the hose, through the manifolds. The influence of variation or nonlinearity due to the rate of penetration, seabed soil resistance, and uplift on the seabed is shown in this work on the 3D nonlinear seabed model. Thus, this research presents novelties which are useful in hose design and manufacturing.

Author Contributions: Conceptualization, C.V.A., J.Y.; methodology, C.V.A., J.Y., F.W.; software, C.V.A., J.Y.; validation, C.V.A., J.Y., F.W.; formal analysis, C.V.A.; investigation, C.V.A., J.Y., F.W.; resources, C.V.A.; data curation, C.V.A.; writing—original draft preparation, C.V.A.; writing—review and editing, C.V.A., J.Y., F.W.; visualization, C.V.A.; supervision, C.V.A., J.Y., F.W.; project administration, C.V.A.; funding acquisition, C.V.A., J.Y. and F.W. All authors have read and agreed to the published version of the manuscript.

Funding: The Department of Engineering, Lancaster University, UK is highly appreciated. In addition, the funding of Overseas Scholarships by Nigeria's NDDC (Niger Delta Development Commission) is also appreciated, as well as the support of Standards Organisation of Nigeria (SON), F.C.T Abuja, Nigeria. We would also like to acknowledge National Natural Science Foundation of China (NSFC) for supporting the Project 51922064 with this study. The article processing charges (APC) for this article was funded by Author 1, with support from MDPI's JMSE.

Institutional Review Board Statement: Not applicable.

Informed Consent Statement: Not applicable.

Data Availability Statement: The raw/processed data required to reproduce these findings cannot be shared at this time, as the data also forms part of an ongoing study.

Acknowledgments: The author acknowledges the technical support from Lancaster University Engineering Department staff. The authors also acknowledge Richard Leeuwenburgh, of Bluewater for permission to use Figure 2. EMSTEC is acknowledged for permission to use Hose Images adapted in our illustration in Figure 6. Also, grateful to Abiodun K. Oyetunji of Lancaster University, for reviewing this manuscript. Lastly, the users support team of the ANSYS and Orcaflex's Orcina is appreciated for technical support, especially Sarah Ellwood of Orcina UK.

Conflicts of Interest: The authors declare no conflict of interest. The funders had no role in the design of the study; in the collection, analyses, or interpretation of data; in the writing of the manuscript, or in the decision to publish the results.

Abbreviations

PC Semi	Paired Column Semisubmersible
3D	Three Dimensional
6DoF	Six Degrees of Freedom
BEM	Boundary Element Method
BM	Bending Moment
CALM	Catenary Anchor Leg Mooring
CCS	Cartesian Coordinate System
DAF	Dynamic Amplification Factor
DoF	Degree of Freedom
fds	Fully Developed Sea
FEA	Finite Element Analysis
FEM	Finite Element Model
FOS	Floating Offshore Structure
FPSO	Floating Production Storage and Offloading
FSO	Floating Storage and Offloading
GoM	Gulf of Mexico
HEV	Hose End Valve
MBC	Marine Breakaway Coupling
MBR	Minimum Bearing Radius
OCIMF	Oil Companies International Marine Forum
PCSemi	Paired Column Semisubmersible
PLEM	Pipeline End Manifold
PIP	Pipe-In-Pipe
RAO	Response Amplitude Operator
SCR	Steel Catenary Riser
SPM	Single Point Mooring
TDP	Touch Down Point
TDZ	Touch Down Zone
TM	Theoretical Model
TTR	Top Tensioned Riser
VIV	Vortex Induced Vibration
VLFS	Very Large Floating Structures

References

1. Trelleborg. Trelleborg Fluid Handling Solutions. Oil & Marine Hoses: Innovation and Safety for Oil & Gas Transfer Systems. In *Trelleborg Oil & Gas Solutions: Oil & Gas Hoses for Enhanced Fluid Transfer Solutions*; Trelleborg: Clemont-Ferrand, France, 2018; Volume 1, pp. 1–30.
2. Bluewater Energy Services. *Buoyed Up: The Future of Tanker Loading/Offloading Operations*; Bluewater Energy Services: Amsterdam, The Netherlands, 2009. Available online: https://www.bluewater.com/wp-content/uploads/2013/04/CALM-Buoy-brochure-English.pdf (accessed on 18 July 2021).
3. The Yokohama Rubber Co., Ltd. *Seaflex Yokohama Offshore Loading & Discharge Hose*; The Yokohama Rubber Co., Ltd.: Hiratsuka, Japan, 2016. Available online: https://www.y-yokohama.com/global/product/mb/pdf/resource/seaflex.pdf (accessed on 19 May 2021).
4. EMSTEC. *EMSTEC Loading & Discharge Hoses for Offshore Moorings*; EMSTEC: Rosengarten, Germany, 2016; Available online: https://denialink.eu/pdf/emstec.pdf (accessed on 29 September 2021).
5. Amaechi, C.V. Single Point Mooring (SPM) Hoses and Catenary Anchor Leg Mooring (CALM) Buoys. LinkedIn Pulse. Published on 26 July 2021. Available online: https://www.linkedin.com/pulse/single-point-mooring-spm-hoses-catenary-anchor-leg-calm-amaechi (accessed on 1 September 2021).
6. Amaechi, C.V.; Wang, F.; Ye, J. Mathematical Modelling of Bonded Marine Hoses for Single Point Mooring (SPM) Systems, with Catenary Anchor Leg Mooring (CALM) Buoy application—A Review. *J. Mar. Sci. Eng.* **2021**, 9.

7. Amaechi, C.V. Development of bonded marine hoses for sustainable loading and discharging operations in the offshore-renewable industry. *J. Pet. Sci. Eng.* **2021**. under review.
8. Amaechi, C.V.; Wang, F.; Xiaonan, H.; Ye, J. Strength of submarine hoses in Chinese-lantern configuration from hydrodynamic loads on CALM buoy. *Ocean Eng.* **2019**, *171*, 429–442. [CrossRef]
9. Amaechi, C.V.; Ye, J.; Hou, X.; Wang, F.-C. Sensitivity Studies on Offshore Submarine Hoses on CALM Buoy with Comparisons for Chinese-Lantern and Lazy-S Configuration OMAE2019-96755. In Proceedings of the 38th International Conference on Ocean, Offshore and Arctic Engineering, Glasgow, Scotland, 9–14 June 2019; American Society of Mechanical Engineers: New York, NY, USA, 2019.
10. Amaechi, C.V.; Wang, F.; Ye, J. An Overview on Bonded Marine Hoses for sustainable fluid transfer and (un)loading operations via Floating Offshore Structures (FOS). *J. Mar. Sci. Eng.* **2021**.
11. Amaechi, C.V. Review on the mechanics and design of marine bonded hoses for CALM buoys. *Ocean Eng.* **2021**.
12. Ye, J.; Cai, H.; Liu, L.; Zhai, Z.; Amaechi, C.V.; Wang, Y.; Wan, L.; Yang, D.; Chen, X.; Ye, J. Microscale intrinsic properties of hybrid unidirectional/woven composite laminates: Part I experimental tests. *Compos. Struct.* **2020**, *262*, 113369. [CrossRef]
13. Amaechi, C.V.; Odijie, C.; Sotayo, A.; Wang, F.; Hou, X.; Ye, J. Recycling of Renewable Composite Materials in the Offshore Industry. *Encycl. Renew. Sustain. Mater.* **2019**, *2*, 583–613. [CrossRef]
14. Amaechi, C.V.; Odijie, C.; Etim, O.; Ye, J. Economic Aspects of Fiber Reinforced Polymer Composite Recycling. *Encycl. Renew. Sustain. Mater.* **2019**, *2*, 377–397. [CrossRef]
15. Tonatto, M.L.; Tita, V.; Amico, S.C. Composite spirals and rings under flexural loading: Experimental and numerical analysis. *J. Compos. Mater.* **2020**, *54*, 2697–2705. [CrossRef]
16. Tonatto, M.L.P.; Tita, V.; Forte, M.M.C.; Amico, S.C. Multi-scale analyses of a floating marine hose with hybrid polyaramid/polyamide reinforcement cords. *Mar. Struct.* **2018**, *60*, 279–292. [CrossRef]
17. Tonatto, M.L.P.; Roese, P.B.; Tita, V.; Forte, M.M.C.; Amico, S.C. Offloading marine hoses: Computational and experimental analyses. In *Marine Composites: Design and Performance*, 1st ed.; Summerscales, J., Graham-Jones, J., Pemberton, R., Eds.; Woodhead Publishing: New York, NY, USA, 2018; Volume 1, pp. 389–416.
18. Tonatto, M.L.P.; Forte, M.M.; Tita, V.; Amico, S. Progressive damage modeling of spiral and ring composite structures for offloading hoses. *Mater. Des.* **2016**, *108*, 374–382. [CrossRef]
19. Tonatto, M.L.P.; Tita, V.; Araujo, R.T.; Forte, M.M.; Amico, S. Parametric analysis of an offloading hose under internal pressure via computational modeling. *Mar. Struct.* **2017**, *51*, 174–187. [CrossRef]
20. Amaechi, C.V. Local tailored design of deep water composite risers subjected to burst, collapse and tension loads. *Ocean Eng.* **2021**. under review.
21. Amaechi, C.V. A review of state-of-the-art and meta-science analysis on composite risers for deep seas. *Ocean Eng.* **2021**. under review.
22. Amaechi, C.V. Development of composite risers for offshore applications with review on design and mechanics. *Ships Offshore Struct.* **2021**. under review.
23. Amaechi, C.V.; Gillett, N.; Odijie, A.C.; Hou, X.; Ye, J. Composite risers for deep waters using a numerical modelling approach. *Compos. Struct.* **2019**, *210*, 486–499. [CrossRef]
24. Amaechi, C.V.; Ye, J. A Numerical Modeling Approach to Composite Risers for Deep Waters. In Proceedings of the 20th International Conference on Composite Structures (ICCS20), Paris, France, 4–7 September 2017; Società Editrice Esculapio: Bologna, Italy, 2017.
25. Amaechi, C.V.; Gillett, N.; Odijie, A.C.; Wang, F.; Hou, X.; Ye, J. Local and Global Design of Composite Risers on Truss SPAR Platform in Deep Waters. In Proceedings of the 5th International Conference on Mechanics of Composites. Instituto Superior de Tecnico, Lisbon, Portugal, 1–4 July 2019; no. 20005. pp. 1–3.
26. Amaechi, C.V. Novel design, hydrodynamics and mechanics of composite risers in oil/gas applications: Case study of marine hoses. Ph.D. Thesis, Lancaster University, Engineering Department, Lancaster, UK, 2021. (in view).
27. Amaechi, C.V. Experimental, analytical and numerical study on CALM buoy hydrodynamic motion response and the hose-snaking phenomenon of the attached marine hoses under water waves. *JMSE* **2021**. under review.
28. Amaechi, C.V. Numerical investigation on mooring line configurations of a Paired Column Semisubmersible for its global performance in deep water condition. *Ocean Eng.* **2021**. under review.
29. Amaechi, C.V. Parametric investigation on tensioner stroke analysis, recoil analysis and disconnect for the marine drilling riser of a Paired Column Semisubmersible under deep water waves. *Ocean Eng.* **2021**. under review.
30. Amaechi, C.V. Dynamic analysis of tensioner model applied on global response of marine riser recoil and disconnect. *Ocean Eng.* **2021**. under review.
31. Odijie, A.C.; Wang, F.; Ye, J. A review of floating semisubmersible hull systems: Column stabilized unit. *Ocean Eng.* **2017**, *144*, 191–202. [CrossRef]
32. Odijie, A.C.; Quayle, S.; Ye, J. Wave induced stress profile on a paired column semisubmersible hull formation for column reinforcement. *Eng. Struct.* **2017**, *143*, 77–90. [CrossRef]
33. Odijie, A.C.; Ye, J. Effect of Vortex Induced Vibration on a Paired-Column SemiSubmersible Platform. *Int. J. Struct. Stab. Dyn.* **2015**, *15*, 8. [CrossRef]

34. Odijie, A.C.; Ye, J. Understanding Fluid-Structure Interaction for high amplitude wave loadings on a deep-draft paired column semi-submersible platform: A finite element approach. In Proceedings of the 4th International Conference on Light Weight Design of Marine Structures, Glasgow, UK, 9–11 November 2015.
35. Odijie, A.C. Design of Paired Column Semisubmersible Hull. Ph.D. Thesis, Lancaster University, Engineering Department, Lancaster, UK, 2016. Available online: https://eprints.lancs.ac.uk/id/eprint/86961/1/2016AgbomeriePhD.pdf (accessed on 14 June 2021).
36. Amaechi, C.V.; Wang, F.; Ye, J. Numerical studies on CALM buoy motion responses, and the effect of buoy geometry cum skirt dimensions with its hydrodynamic waves-current interactions. *Ocean Eng.* **2021**. under review.
37. Amaechi, C.V. Numerical assessment of offshore hose load response during reeling and free-hanging operations under ocean waves. *Ocean Eng.* **2021**. under review.
38. Amaechi, C.V. Analytical cum numerical solutions on added mass and damping of a CALM buoy towards understanding the fluid-structure interaction of marine bonded hose under random waves. *Mar. Struct.* **2021**. under review.
39. Amaechi, C.V.; Wang, F.; Ye, J. Understanding the fluid-structure interaction from wave diffraction forces on CALM buoys: Numerical and analytical solutions. *Ships Offshore Struct.* **2021**. under review.
40. Wang, F.; Chen, J.; Gao, S.; Tang, K.; Meng, X. Development and sea trial of real-time offshore pipeline installation monitoring system. *Ocean Eng.* **2017**, *146*, 468–476. [CrossRef]
41. Wang, F.-C.; Wang, J.; Tang, K. A finite element based study on lowering operation of subsea massive structure. *China Ocean Eng.* **2017**, *31*, 646–652. [CrossRef]
42. Lenci, S.; Callegari, M. Simple analytical models for the J-lay problem. *Acta Mech.* **2005**, *39*, 23–39. [CrossRef]
43. Gong, S.; Xu, P.; Bao, S.; Zhong, W.; He, N.; Yan, H. Numerical modelling on dynamic behaviour of deepwater S-lay pipeline. *Ocean Eng.* **2014**, *88*, 393–408. [CrossRef]
44. Trapper, P.A. Static analysis of offshore pipe-lay on flat inelastic seabed. *Ocean Eng.* **2020**, *213*, 107673. [CrossRef]
45. Gong, S.; Xu, P. Influences of pipe-soil interaction on dynamic behaviour of deepwater S-lay pipeline under random sea states. *Ships Offshore Struct.* **2017**, *12*, 3–370. [CrossRef]
46. Sagrilo, L.V.S.; Siqueira, M.Q.; Ellwanger, G.B.; Lima, E.C.P.; Ferreira, M.D.A.S.; Mourelle, M.M. A coupled approach for dynamic analysis of CALM systems. *Appl. Ocean Res.* **2002**, *24*, 47–58. [CrossRef]
47. Santala, M.J.; Wang, H.; Huang, Z.J.; Yung, T.W. Component Approach for Confident Predications of Deepwater CALM Buoy Coupled Motions—Part 2: Analytical Implementation. In Proceedings of the 24th International Conference on Offshore Mechanics and Arctic Engineering, Halkidiki, Greece, 12–17 June 2005; OMAE2005-67140. The American Society of Mechanical Engineers: New York, NY, USA, 2005; pp. 367–375. Available online: https://citeseerx.ist.psu.edu/viewdoc/download?doi=10.1.1.1078.941&rep=rep1&type=pdf (accessed on 11 September 2021). [CrossRef]
48. Kang, Y.; Sun, L.; Kang, Z.; Chai, S. Coupled Analysis of FPSO and CALM Buoy Offloading System in West Africa. In Proceedings of the 33rd International Conference on Offshore Mechanics and Arctic Engineering, San Francisco, CA, USA, 8–13 June 2014; OMAE2014-23118; Volume 8A: Ocean Engineering; V08AT06A010. ASME. The American Society of Mechanical Engineers: New York, NY, USA, 2014; pp. 1–11. Available online: https://www.researchgate.net/profile/Shuhong-Chai/publication/278675856_Coupled_analysis_of_FPSO_and_CALM_buoy_offloading_system_in_West_Africa/links/5582ce9708ae12bde6e63129/Coupled-analysis-of-FPSO-and-CALM-buoy-offloading-system-in-West-Africa.pdf (accessed on 11 September 2021). [CrossRef]
49. Cozijn, J.L.; Bunnik, T.H.J. Coupled Mooring Analysis for a Deep Water CALM Buoy. In Proceedings of the 23rd International Conference on Offshore Mechanics and Arctic Engineering (OMAE), Volume 1, Parts A and B; ASME. Vancouver, BC, USA, 20–25 June 2014; The American Society of Mechanical Engineers: New York, NY, USA, 2004; pp. 663–673. [CrossRef]
50. Le Cunff, C.; Ryu, S.; Duggal, A.; Ricbourg, C.; Heurtier, J.; Heyl, C.; Liu, Y.; Beauclair, O. Derivation of CALM Buoy coupled motion RAOs in Frequency Domain and Experimental Validation. In Proceedings of the 17th International Society of Offshore and Polar Engineering Conference, Lisbon, Portugal, 1–6 July 2007; no. 2007-NaN-594. International Society of Offshore and Polar Engineers (ISOPE): Cupertino, CA, USA, 2007; pp. 1–8. Available online: https://www.sofec.com/wp-content/uploads/white_papers/2007-ISOPE-Derivation-of-CALM-Buoy-Coupled-Motion-RAOs-in-Frequency-Domain.pdf (accessed on 29 September 2021).
51. Le Cunff, C.; Ryu, S.; Heurtier, J.-M.; Duggal, A.S. Frequency-Domain Calculations of Moored Vessel Motion Including Low Frequency Effect. In Proceedings of the 27th International Conference on Offshore Mechanics and Arctic Engineering, Estoril, Portugal, 15–20 June 2008; OMAE2008-57632. Volume 1: Offshore Technology; ASME. The American Society of Mechanical Engineers: New York, NY, USA, 2008; pp. 689–696. [CrossRef]
52. Williams, N.A.; McDougal, W.G. Experimental Validation Of A New Shallow Water Calm Buoy Design. In Proceedings of the 32nd International Conference on Ocean, Offshore and Arctic Engineering, Volume 1: Offshore Technology; V001T01A070. ASME. Nantes, France, 9–14 June 2013; The American Society of Mechanical Engineers: New York, NY, USA, 2013; pp. 1–6. [CrossRef]
53. Berhault, C.; Guerin, P.; le Buhan, P.; Heurtier, J.M. Investigations on Hydrodynamic and Mechanical Coupling Effects for Deepwater Offloading Buoy. In Proceedings of the 14th International Offshore and Polar Engineering Conference, Toulon, France, 23–28 May 2004; International Society of Offshore and Polar Engineers (ISOPE): Cupertino, CA, USA; Volume 1, pp. 374–379. Available online: https://onepetro.org/ISOPEIOPEC/proceedings-abstract/ISOPE04/All-ISOPE04/ISOPE-I-04-363/10313 (accessed on 11 September 2021).

54. Randolph, M.; Quiggin, P. Non-linear hysteretic seabed model for catenary pipeline contact. In Proceedings of the 28th International Conference on Ocean, Offshore and Arctic Engineering Proceedings, Honolulu, Hawaii, 31 May–5 June 2009; Volume 3: Pipeline and Riser Technology. The American Society of Mechanical Engineers: New York, NY, USA, 2009; pp. 145–154. Available online: https://www.orcina.com/wp-content/uploads/OMAE2009-79259.pdf (accessed on 11 September 2021). [CrossRef]
55. Kimiaei, M.; Randolph, M.; Ting, I. A parametric study on effects of environmental loadings on fatigue life of steel catenary risers (using a nonlinear cyclic riser-soil interaction model). In Proceedings of the ASME 2010 29th International Conference on Ocean, Offshore and Arctic Engineering, Shanghai, China, 6–11 June 2010; Volume 5: Parts A and B. The American Society of Mechanical Engineers: New York, NY, USA, 2010; pp. 1085–1093, OMAE2010-21153; ASME. [CrossRef]
56. Quéau, L.M.; Kimiaei, M.; Randolph, M.F. Analytical estimation of static stress range in oscillating steel catenary risers at touchdown areas and its application with dynamic amplification factors. *Ocean Eng.* **2014**, *88*, 63–80. [CrossRef]
57. Quéau, L.M.; Kimiaei, M.; Randolph, M.F. Dynamic Amplification Factors for Response Analysis of Steel Catenary Risers at Touch Down Areas. In Proceedings of the 21st International Conference on Offshore and Polar Engineering (ISOPE), Maui, HI, USA, 19–24 June 2011; International Society of Offshore and Polar Engineers (ISOPE): Cupertino, CA, USA; Volume 8, pp. 1–5. Available online: https://onepetro.org/ISOPEIOPEC/proceedings-abstract/ISOPE11/All-ISOPE11/ISOPE-I-11-233/13224 (accessed on 11 September 2021).
58. Quéau, L.M.; Kimiaei, M.; Randolph, M.F. Sensitivity studies of SCR fatigue damage in the touchdown zone using an efficient simplified framework for stress range evaluation. *Ocean Eng.* **2015**, *96*, 295–311. [CrossRef]
59. Sun, L.; Zhang, X.; Kang, Y.; Chai, S. Motion response analysis of FPSO's CALM buoy offloading system. In Proceedings of the 34th International Conference on Ocean, Offshore and Arctic Engineering, OMAE2015-41725; Prof. Robert F. Beck Honoring Symposium on Marine Hydrodynamics. V011T12A008. St. John's, NL, Canada, 31 May–5 June 2015; American Society of Mechanical Engineers: New York, NY, USA, 2015; Volume 11, pp. 1–7. [CrossRef]
60. Salem, G.; Ryu, S.; Duggal, A.S.; Raju; Datla, V. Linearization of Quadratic Drag to Estimate CALM Buoy Pitch Motion in Frequency-Domain and Experimental validation. *J. Offshore Mech. Arct. Eng.* **2012**, *134*, 3–8. [CrossRef]
61. Cozijn, H.; Uittenbogaard, R.; Brake, E.T. Heave, Roll and Pitch Damping of a Deepwater CALM Buoy with a Skirt. In Proceedings of the 15th International Society of Offshore and Polar Engineering Conference, Seoul, Korea, 19–24 June 2005; International Society of Offshore and Polar Engineers (ISOPE): Cupertino, CA, USA; Volume 8, pp. 388–395. Available online: https://www.researchgate.net/publication/267364857_Heave_Roll_and_Pitch_Damping_of_a_Deepwater_CALM_Buoy_with_a_Skirt (accessed on 11 September 2021).
62. Duggal, A.; Ryu, S. The dynamics of deepwater offloading buoys. In *WIT Transactions on The Built Environment*; WIT Press: Southampton, UK, 2005. Available online: https://www.witpress.com/elibrary/wit-transactions-on-the-built-environment/84/15733 (accessed on 11 September 2021). [CrossRef]
63. Ryu, S.; Duggal, A.S.; Heyl, C.N.; Liu, Y. Prediction of Deepwater Oil Offloading Buoy Response and Experimental Validation. *Int. J. Offshore Polar Eng.* **2006**, *16*, 1–7. Available online: https://www.sofec.com/wp-content/uploads/white_papers/2006-ISOPE-Prediction-of-DW-Oil-Offloading-Buoy-Response.pdf (accessed on 11 September 2021).
64. Morison, J.R.; O'Brien, M.P.; Johnson, J.W.; Schaaf, S.A. The Force Exerted by Surface Waves on Piles. *J. Pet. Technol.* **1950**, *189*, 149–154. [CrossRef]
65. Løtveit, S.A.; Muren, J.; Nilsen-Aas, C.K.O. *Bonded Flexibles–State of the Art Bonded Flexible Pipes; 26583U-1161480945-354, Revision 2.0, Approved on 17.12.2018; Prepared for PSA Norway*; 4subsea: Asker, Norway, 2018; pp. 1–75. Available online: https://www.4subsea.com/wp-content/uploads/2019/01/PSA-Norway-State-of-the-art-Bonded-Flexible-Pipes-2018_4Subsea.pdf (accessed on 17 June 2021).
66. Muren, J.; Caveny, K.; Eriksen, M.; Viko, N.G.; MÜLler-Allers, J.; JØRgen, K.U. *Un-bonded Flexible Risers–Recent Field Experience and Actions for Increased Robustness. 0389-26583-U-0032, Revision 5.0; Prepared for PSA Norway*; 4subsea: Asker, Norway, 2013; Volume 2, pp. 1–78. Available online: https://www.ptil.no/contentassets/c2a5bd00e8214411ad5c4966009d6ade/un-bonded-flexible-risers--recent-field-experience-and-actions--for-increased-robustness.pdf (accessed on 17 June 2021).
67. Goff, R.; Kay, J. *Investigations Into the Immediate and Underlying Causes of Failures of Offshore Riser Emergency Shutdown Valves*; Health and Safety Laboratory; SK17 9JN; HSE Books: Buxton, UK, 2015. Available online: https://www.hse.gov.uk/research/rrpdf/rr1072.pdf (accessed on 1 September 2021).
68. Goff, R.J. earning from the Causes of Failures of Offshore Riser Emergency Shutdown Valves. Symposium Series Number 161, Hazards 26. 2016. Available online: https://www.icheme.org/media/11788/hazards-26-paper-51-learning-from-the-causes-of-failures-of-offshore-riser-emergency-shutdown-valves.pdf (accessed on 1 September 2021).
69. Fergestad, D.; Løtveit, S.A. *and Løtveit, S.A. Handbook on Design and Operation of Flexible Pipes*, MARINTEK/NTNU/4Subsea, 3rd ed.; Sintef: Trondheim, Norway, 2017. Available online: https://www.4subsea.com/wp-content/uploads/2017/07/Handbook-2017_Flexible-pipes_4Subsea-SINTEF-NTNU_lo-res.pdf (accessed on 25 August 2021)ISBN 978-82-7174-285-0.
70. Barltrop, N.D.P.; Adams, A.J. *Dynamics of Fixed Marine Structures*, 3rd ed.; Butterworth Heinemann: Oxford, UK, 1991.
71. Barltrop, N.D.P. *Floating Structures: A Guide for Design and Analysis*; Oilfield Publications Limited (OPL): Herefordshire, UK, 1998; Volume 1.
72. Amaechi, C.V. Investigation on hydrodynamic characteristics, wave-current interaction and sensitivity analysis of submarine hoses attached to a CALM buoy. *JMSE* **2021**. under review.

73. Orcina. *OrcaFlex Manual, Version 9.8a*; Orcina Ltd.: Ulverton, UK, 2014.
74. Orcina. *Seabed Nonlinear Soil Model Theory. Orcaflex theory documentation, version 11.0f*; Orcina: Ulverston, UK, 2021. Available online: https://www.orcina.com/webhelp/OrcaFlex/Content/html/Seabednonlinearsoilmodeltheory.htm (accessed on 2 September 2021).
75. ANSYS. *Aqwa User's Manual, Release 18.2*; ANSYS Inc.: Canonsburg, PA, USA, 2017.
76. ANSYS. *Aqwa Theory Manual, Release 18.2*; ANSYS Inc.: Canonsburg, PA, USA, 2017.
77. Ibinabo, I.; Tamunodukobipi, D.T. Determination of the Response Amplitude Operator(s) of an FPSO. *Engineering* **2019**, *11*, 541–556. [CrossRef]
78. Baghfalaki, M.; Das, S.K.; Das, S.N. Analytical model to determine response amplitude operator of a floating body for coupled roll and yaw motions and frequency based analysis. *Int. J. Appl. Mech.* **2012**, *4*, 1–20. [CrossRef]
79. Das, S.K.; Baghfalaki, M. Mathematical modelling of response amplitude operator for roll motion of a floating body: Analysis in frequency domain with numerical validation. *J. Marine. Sci. Appl.* **2014**, *13*, 143–157. [CrossRef]
80. Sarpkaya, T. *Wave Forces on Offshore Structures*, 1st ed.; Cambridge University Press: New York, NY, USA, 2014.
81. O'Donoghue, T.; Halliwell, A.R. Floating Hose-Strings Attached to a CALM Buoy. In In Proceedings of the Offshore Technology Conference, Houston, TX, USA, 2–5 May 1988; OTC 5717. pp. 313–320. [CrossRef]
82. Bree, J.; Halliwell, A.R.; O'Donoghue, T. Snaking of floating marine oil hose attached to SPM buoy. *J. Eng. Mech.* **1989**, *115*, 2–265. [CrossRef]
83. O'Donoghue, T.; Halliwell, A.R. Vertical bending moments and axial forces in a floating marine hose-string. *Eng. Struct.* **1990**, *12*, 4–124. [CrossRef]
84. O'Donoghue, T. The Dynamic Behaviour of a Surface Hose Attached to a CALM Buoy. Ph.D. Thesis, Department of Offshore Engineering, Heriot-Watt University, Edinburgh, UK. Available online: https://www.ros.hw.ac.uk/bitstream/10399/1045/1/O%27DonoghueT_0587_epsBL.pdf (accessed on 1 September 2021).
85. Brown, M.J.; Elliott, L. Two-dimensional dynamic analysis of a floating hose string. *Appl. Ocean Res.* **1988**, *10*, 20–34. [CrossRef]
86. Brown, M.J. Mathematical Model of a Marine Hose-String at a Buoy—Part 1—Static Problem. In *Offshore and Coastal Modelling*; Dyke, P., Moscardini, A.O., Robson, E.H., Eds.; Springer: London, UK, 1985; pp. 251–277. [CrossRef]
87. Brown, M.J. Mathematical Model of a Marine Hose-String at a Buoy—Part 2—Dynamic Problem. In *Offshore and Coastal Modelling*; Dyke, P., Moscardini, A.O., Robson, E.H., Eds.; Springer: London, UK, 1985; pp. 279–301. [CrossRef]
88. DNVGL. *DNVGL-RP-F205 Global Performance Analysis of Deepwater Floating Structures*; Det Norske Veritas & Germanischer Lloyd: Oslo, Norway, 2017.
89. DNVGL. *DNVGL-RP-N103 Modelling and Analysis of Marine Operations*; Det Norske Veritas & Germanischer Lloyd: Oslo, Norway, 2017.
90. DNVGL. *DNVGL-OS-E403 Offshore Loading Buoys*; Det Norske Veritas & Germanischer Lloyd: Oslo, Norway, 2015.
91. ABS. *Rules For Building And Classing—Single Point Moorings*; American Bureau of Shipping: New York, NY, USA, 2017; Volume 2017.
92. OCIMF. *Guide to Manufacturing and Purchasing Hoses for Offshore Moorings (GMPHOM)*; Witherby Seamanship International Ltd.: Livingstone, UK, 2009.
93. OCIMF. *Guideline for the Handling, Storage, Inspection and Testing of the Hose*, 2nd ed.; Witherby & Co. Ltd.: London, UK, 1995.
94. OCIMF. *Single Point Mooring Maintenace and Operations Guide (SMOG)*; Witherby & Co. Ltd.: London, UK, 1995.
95. Timoshenko, S.P. On the correction of shear of the differential equation for transverse vibrations of prismatic bars. *Philos. Mag.* **1921**, *41*, 744–746. [CrossRef]
96. Timoshenko, S.P. On the transverse vibrations of bars of uniform cross-section. *Philos. Mag.* **1921**, *43*, 125–131. [CrossRef]
97. Hirdaris, S.E.; Lees, A.W. A conforming unified finite element formulation for the vibration of thick beams and frames. *Int. J. Numer. Methods Eng.* **2004**, *62*, 579–599. [CrossRef]
98. Sparks, C.P. *Fundamentals of Marine Riser Mechanics: Basic Principles and Simplified Analyses*, 2nd ed.; PennWell Books: Tulsa, OK, USA, 2018.
99. Dareing, D.W. *Mechanics of Drillstrings and Marine Risers*, 1st ed.; ASME Press: New York, NY, USA, 2012. [CrossRef]
100. Irvine, H.M. *Cable Structures*; MIT Press: Cambridge, MA, USA, 1981.
101. Bai, Y.; Bai, Q. *Subsea Engineering Handbook*; Elsevier: Oxford, UK, 2010.
102. Bai, Y.; Bai, Q. *Subsea Pipelines and Risers*, 1st ed.; Elsevier: Oxford, UK, 2005.
103. Brebbia, C.A.; Walker, S. *Dynamic Analysis of Offshore Structures*, 1st ed.; Newnes-Butterworth & Co. Publishers Ltd.: London, UK, 1979.
104. Chandrasekaran, S. *Dynamic Analysis and Design of Offshore Structures*, 1st ed.; Springer: New Delhi, India, 2015.
105. Wilson, J.F. *Dynamics of Offshore Structures*, 2nd ed.; John Wiley and Sons: Hoboken, NJ, USA, 2003.
106. Chakrabarti, S.K. *Handbook of Offshore Engineering*; Elsevier: Oxford, UK, 2005; Volume 1.
107. Chakrabarti, S.K. *Handbook of Offshore Engineering*; Elsevier: Oxford, UK, 2006; Volume 2.
108. Bishop, R.E.D.; Price, W.G. *Hydroelasticity of Ships*; Cambridge University Press: New York, NY, USA, 2005.
109. Newman, J.N. , *Marine Hydrodynamics*; 1999 Repri.; MIT Press: London, UK, 1977.
110. Faltinsen, O.M. *Sea Loads on Ships and Offshore Structures*; 1995 Repri.; Cambridge University Press: Cambridge, UK, 1990.
111. Wichers, I.J. *Guide to Single Point Moorings*; WMooring Inc.: Houston, TX, USA, 2013.

112. Hirdaris, S.E.; Bai, W.; Dessi, D.; Ergin, A.; Gu, X.; Hermundstad, O.A.; Huijsmans, R.; Iijima, K.; Nielsen, U.D.; Parunov, J.; et al. Loads for use in the design of ships and offshore structures. *Ocean Eng.* **2014**, *78*, 131–174. [CrossRef]
113. Hasselmann, K.; Barnett, T.P.; Bouws, E.; Carlson, H.; Cartwright, D.E.; Enke, K.; Ewing, J.A.; Gienapp, H.; Hasselmann, D.E.; Kruseman, P.; et al. Measurements of wind-wave growth and swell decay during the Joint North Sea Wave Project (JONSWAP). In *Ergänzungsheft zur Dtsch. Hydrogr. Z. -Hydraulic Engineering Reports; Ergänzungsheft 8-12; Reihe Vol. A80, Issue 12*; 1973; Volume 12, pp. 1–90. Deutches Hydrographisches Institut: Hamburg, Germany. Available online: http://resolver.tudelft.nl/uuid:f204e188-13b9-49d8-a6dc-4fb7c20562fc (accessed on 4 March 2021).
114. Pierson, W.J.; Moskowitz, L. A proposed spectral form for fully developed wind seas based on the similarity theory of SA Kitaigorodskii. *J. Geophys. Res. Space Phys.* **1964**, *69*, 5181–5190. [CrossRef]
115. Chakrabarti, S.K. Technical Note: On the formulation of Jonswap spectrum. *Appl. Ocean Res.* **1984**, *6*, 175–176. [CrossRef]
116. Isherwood, R.M. Technical Note: A revised parameterisation of the Jonswap spectrum. *Appl. Ocean Res.* **1987**, *9*, 47–50. [CrossRef]
117. Roveri, F.E.; Volnei, S.; Sagrilo, L.; Cicilia, F.B. A Case Study on the Evaluation of Floating Hose Forces in a C.A.L.M. System. In Proceedings of the 12th International Offshore and Polar Engineering Conference, Kitakyushu, Japan, 26–31 May 2002; International Society of Offshore and Polar Engineers (ISOPE): Cupertino, CA, USA; Volume 3, pp. 190–197.
118. Wang, D.; Sun, S. Study of the Radiation Problem for a CALM Buoy with Skirt. *Sh. Build. China* **2015**, *56*, 95–101.
119. Amaechi, C.V. Effect of marine riser integration for characteristic motion response studies on a Paired Column Semisubmersible in deep waters. *Mar. Struct.* **2021**. under review.
120. Amaechi, C.V. Numerical study on plastic deformation, plastic strains and bending of tubular pipes. *Inventions* **2021**. under review.
121. Wang, F. Effective design of submarine pipe-in-pipe using Finite Element Analysis. *Ocean Eng.* **2018**, *153*, 23–32. [CrossRef]
122. Wang, F.; Han, L. Analytical behaviour of carbon steel-concrete-stainless steel double skin tube (DST) used in submarine pipeline structure. *Mar. Struct.* **2019**, *63*, 99–116. [CrossRef]
123. Wang, F.; Han, L.; Li, W. Analytical behavior of CFDST stub columns with external stainless steel tubes under axial compression. *Thin-Walled Struct.* **2018**, *127*, 756–768. [CrossRef]
124. Wang, J.-T.; Wang, F.-C. Analytical behavior of built-up square concrete-filled steel tubular columns under combined preload and axial compression. *Steel Compos. Struct.* **2021**, *38*, 617–635. [CrossRef]